Scholars' Mine

Doctoral Dissertations

Student Theses and Dissertations

2014

Development of a flat-panel x-ray source

Edwin Joseph Grant

Follow this and additional works at: https://scholarsmine.mst.edu/doctoral_dissertations

Part of the Nuclear Engineering Commons

Department: Nuclear Engineering and Radiation Science

Recommended Citation

DEVELOPMENT OF A FLAT-PANEL X-RAY SOURCE

by

EDWIN JOSEPH GRANT

A DISSERTATION

Presented to the Faculty of the Graduate School of the

MISSOURI UNIVERSITY OF SCIENCE AND TECHNOLOGY

In Partial Fulfillment of the Requirements for the Degree

DOCTOR OF PHILOSOPHY

in

NUCLEAR ENGINEERING

2014

Approved by
Hyoung Koo Lee, Advisor
Carlos H. Castano
Ayodeji B. Alajo
Xin Liu
Muthanna H. Al-Dahhan

ABSTRACT

A novel flat-panel transmission type X-ray source was developed for both medical and industrial use. Depending on the geometry of the given situation, the flat-panel X-ray source could be used in tomography, radiography or tomosynthesis. Furthermore, the unit could be used as a portable X-ray scanner or an integral part of an existing detection system. The design incorporates a field emission cathode made of ultra-nanocrystalline diamonds (UNCD) doped with nitrogen. These field emitters show good electron output at low power and can be deposited over large areas as is the case with carbon nanotube "forest" (CNT) cathodes. This work presents the first generation of the UNCD based FEA prototype which was manufactured at the Center of Nanoscale Material, within Argonne National Laboratory, with standard microfabrication techniques. The prototype is a 3×3 pixel field emission array (FEA), with a pixel size of 225 μm by 225 μm and a pitch of 500 μm. The fabricated cathode was developed using a microfabrication process which allows for individual electrically addressable UNCD gated arrays on-chip which demonstrated monolithic integration of the electron extraction grid.

The transmission target consists of tungsten for X-ray generation, which is sputtered directly upon a thin aluminum sheet as an X-ray filter. A low voltage power supply allows for electron extraction between the cathode and the grid; while a high voltage power supply accelerates the electrons towards the anode. A low energy X-ray high purity germanium detector (HPGe) is mounted outside of the vacuum chamber for X-ray detection and measurement.

iv

ACKNOWLEDGMENTS

ACKNOWLEDGMENTS

TABLE OF CONTENTS

LIST OF ILLUSTRATIONS

LIST OF TABLES

1. INTRODUCTION

1.1. HISTORY OF X-RAY SOURCES

In 1855 the first gas discharge tube was created by Heinrich Geissler, and these early tubes would lead the way for the development of items such as neon signs, cathode ray tubes, and X-ray sources. Later, William Crookes modified the Geissler tube which included incorporating a lower pressure inside of the chamber and in doing so made it possible to identify the X-ray. By increasing the vacuum inside of the chamber the mean free path of the yet to be identified electron increased allowing for higher kinetic energy electrons. In 1895, Wilhelm Rontgen identified the X-ray by accident when a barium platinocyanide photographic plate started to twinkle from the other side of the laboratory [1]. In fact, Wilhelm took the first radiographic X-ray image, days after the discovery of the X-ray, of his wife's hand as seen in Figure 1.1.

Figure 1.1. First X-ray Radiographic Image. [1]

With the identification of the X-ray a new boom of X-ray technology followed in its wake. In 1913, William Coolidge designed the first tube which included an electric current on the cathode that induced thermionic electron emission. Even to this day, nearly all manufactured X-ray tubes still use hot cathode technology. Another emerging technological design (~1900) was the rotating anode design to help disperse large heat loads being deposited on the anode which is generated from the transformation of kinetic energy of the electron into thermal energy. However, a sealed, properly greased rotating shaft sealed within an evacuated glass envelope was not easy to manufacture. The first commercially available rotating anode tube was created by Philips, called the Rotalix Metalix [2]. Current designs which help further remove heat from the X-ray tube, include pumping oil over the anode assembly's housing. Interestingly, the first water cooled X-ray tube was patented in 1899 by Carl Muller [3]. By integrating all of these design changes to the Coolidge tube, we would end up with the current design of the modern X-ray tube.

1.2. FUTURE OF X-RAY TECHNOLOGY

Since the discovery of X-rays by Wilhelm Roentgen in 1895, we have greatly benefited from their properties. However, even after 100 years, the general operational design for X-ray tubes has not been changed from the original idea of producing X-rays from a single focal spot. When imaging with a conventional X-ray tube, X-ray photons generated from the single focal spot constitute a wide diverging beam, which causes geometric distortion of patient anatomy or internal 3D structures of imaged objects for non-destructive evaluation (NDE) due to magnification. To reduce this unwanted effect, the X-ray tube is usually positioned away from the patient (up to ~ 6 feet) when imaging thick parts of the body. This requires higher X-ray intensity from the X-ray tube as the distance increases, worsening the heat deposition problem of conventional X-ray tubes. In search of innovative solutions to the problems of the conventional X-ray tube, we propose a new approach of X-ray generation using millions of micro X-ray tube cells in a 2D array format such that each X-ray cell corresponds to a pixel in an X-ray image. Figure 1.2 shows the schematic diagram of the proposed X-ray source. Each of the cells uses field emission or cold cathode film technology for electron production [4-5].
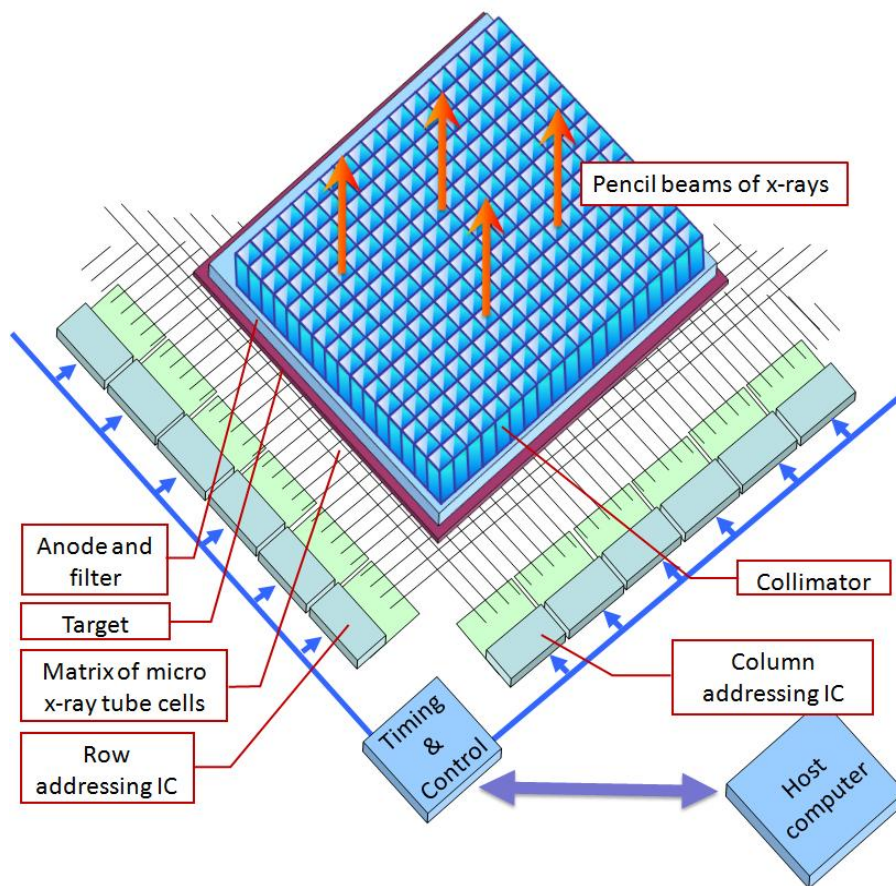
Figure 1.2. Simplified schematic of a flat-panel X-ray source.

Each cell can be addressed independently, making it possible to shape the X-ray beam and spatially modulate the X-ray intensity as needed. Since our device produces a parallel beam, no artifacts due to geometric magnification will occur, which allows making the source-to-detector distance as short as physically possible. This in turns allows imaging with lower intensity X-rays in a smaller space, compared to the case of the conventional X-ray tube. Also, the reduced X-ray intensity causes less heat problems as opposed to conventional X-ray tubes. The heat generated from a cell is spread and dissipated over the entire area of the anode plate; thus, a metal plate with good characteristics both in electrical and thermal conductivities, such as a copper or aluminum plate, would be desirable. The thickness of the anode plate should be thin enough to not deteriorate high-energy photon intensity but thick enough to filter out low-energy photons.

Similar operational designs by other research groups have been devised which incorporated multiple X-ray sources in linear arrays, with or without field emission cathodes. A 25 mm-spaced bilinear source, composed of a 2×4 arrangement of dispenser cathode emitters with a tungsten anode, has been built and operated for 100 hours without failure [6]. Another 1D array design, based on 25 nodes with a source-to-source spacing of approximately 2.25 cm has been constructed and tested [7]. Both of these designs employed a small angle reflection anode. For ease of fabrication, high spatial resolution, and better X-ray emission efficiency, we propose to utilize transmission X-rays within our design. In a transmission source, the electron beam direction and the X-ray emission direction are the same, and an X-ray cell can be made small enough to produce a narrow pencil beam of X-ray for every pixel in an image. Our design incorporates a thin layer of nitrogen-incorporated ultra-nano-crystalline diamond (N-UNCD) as the electron source. N-UNCD technology was developed by collaboration between Argonne National Laboratory and NASA [5]. This material allows for easier fabrication and better, more stable electron emission properties than comparable electron field emitters such as carbon nanotubes [8]. By using micro-fabrication technology found in standard flat-panel LCD or flat-panel radiation imaging detectors, a 2D array of X-ray cells with a cell pitch of 50 μm-200 μm can be manufactured on scales up to 17" by 17". The concept of a flat-panel micro X-ray source is new in the field of X-ray generation in both non-destructive evaluation (NDE) and medical imaging and will be the future of X-ray technology.

2. X-RAY PRODUCTION PRINCIPLES

2.1. COMPONENTS OF A TYPICAL X-RAY SOURCE

A typical X-ray source consists of a glass envelope in which a cathode and anode is placed inside and has a high voltage bias, typically 30 kVp to 150 kVp, to accelerate the electrons to some needed potential, as seen in Figure 2.1. It also can be noted that an operating X-ray tube with a 100 kVp bias will yield a maximum X-ray energy of 100 keV. The operational pressure inside of the glass envelope must be lower than 10^{-5} Torr, else the accelerating electrons will experience many collisions with the air molecules and hinder X-ray generation performance [9]. Also, the X-ray source includes a rotor and stator, which spins the anode at a specific frequency to allow for passive cooling of the anode target by spreading the heat generation to a larger area. Without the increase in useable focal spot size, the target could melt or have other physical damage such as pitting.
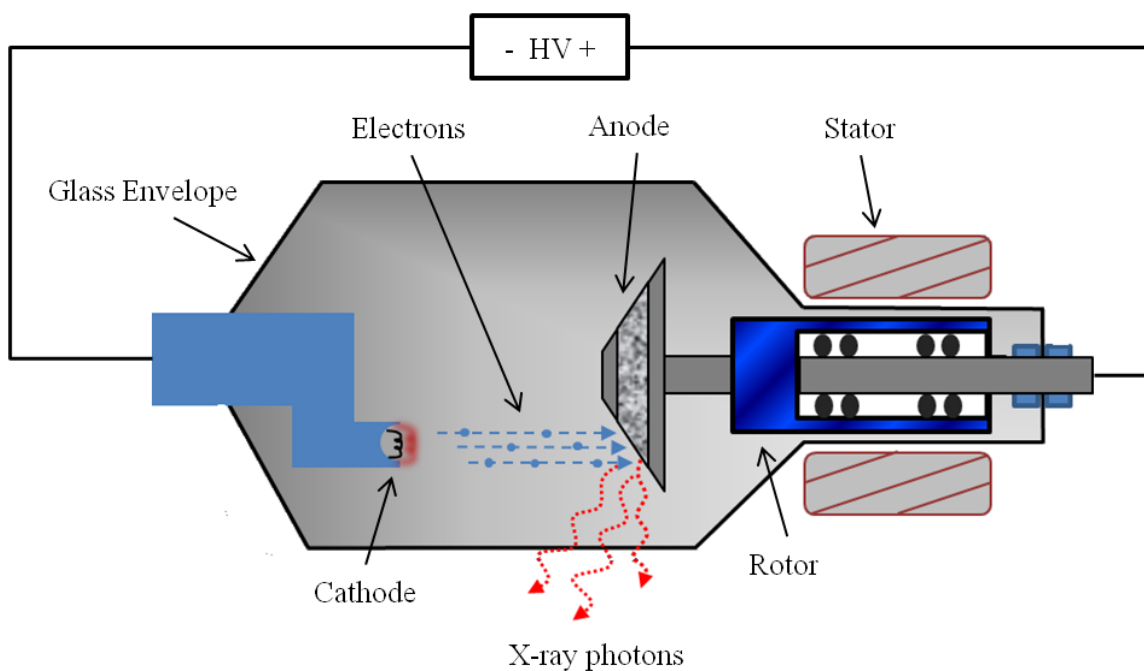
Figure 2.1. Schematic diagram of a typical X-ray source.

2.1.1. Electron Generation.   In general, electrons are extracted from a metallic filament which is heated to approximately $2000°C$. The heating of the filament is needed to help lower the work function of the cathode material and thus allows the electrons to easily surpass the limiting binding potential and accelerate towards the anode. The outer most valence shell of electrons within the metal is somewhat free to move around, and these electrons can leave the metal surface if a strong enough force is given to the electron. This excess amount of energy needed to liberate electrons is provided in the form of thermal energy applied to the cathode. The added kinetic energy to the cathode atoms allows for some of the valence shell electrons to spill or "boil" off of the metallic surface. Quantifying the flow of these electrons is seen by equation 1,

$$J_S = AT^2 e^{\left(-\frac{\phi}{kT}\right)}$$

(1)

where A is the Richardson constant and equal to $4\pi mek^2/h^3$; such that m is the mass of an electron, k is the Boltzmann constant, T is the temperature of the metal, ϕ is the work function of the material and h is Planck's constant. Thus, the thermionic emission is strongly dependent on the temperature and material used for the cathode. This is why metals, such as tungsten, are used because of their high melting temperature.

The use of a hot cathode, to extract electrons, is called thermionic emission, as introduced with the Coolidge tube. For example, hot cathodes essentially operate similar to filaments on old light bulbs, and once you heat up the filament, visible light is emitted from the bulb. One downside of using thermionic emission is that the devices need high power to heat the filament up to operating temperatures, and it takes time to cool down which limits cycling time and overall lifetime of the device.

Another aspect for electron generation design is the electron focusing optics. A focusing cup is generally used to confine the emitted "cloud" of electrons from the cathode filament. The shape of the focusing cup is convex in nature, and with a small negative bias, it helps minimize the negative static charge of the electrons; which makes them want to disperse into a divergent beam.

2.1.2. X-Ray Generation.   There are two key methods for generating X-rays: Bremsstrahlung radiation and characteristic X-rays.   However, two separate physical events are occurring and characteristic X-ray generation is shown below in Figure 2.2. The incoming electron, from the cathode, will strike a bound electron, within a target atom, with enough energy to dislodge the K-shell electron, producing a secondary electron.   On average, approximately 7-8 secondary electrons are produced from a single primary electron [10].   To fill in the gap created by the K-shell vacancy, a higher shell electron will jump down and, in doing so, will emit an X-ray with a kinetic energy equal to the difference between the electron shell potentials.
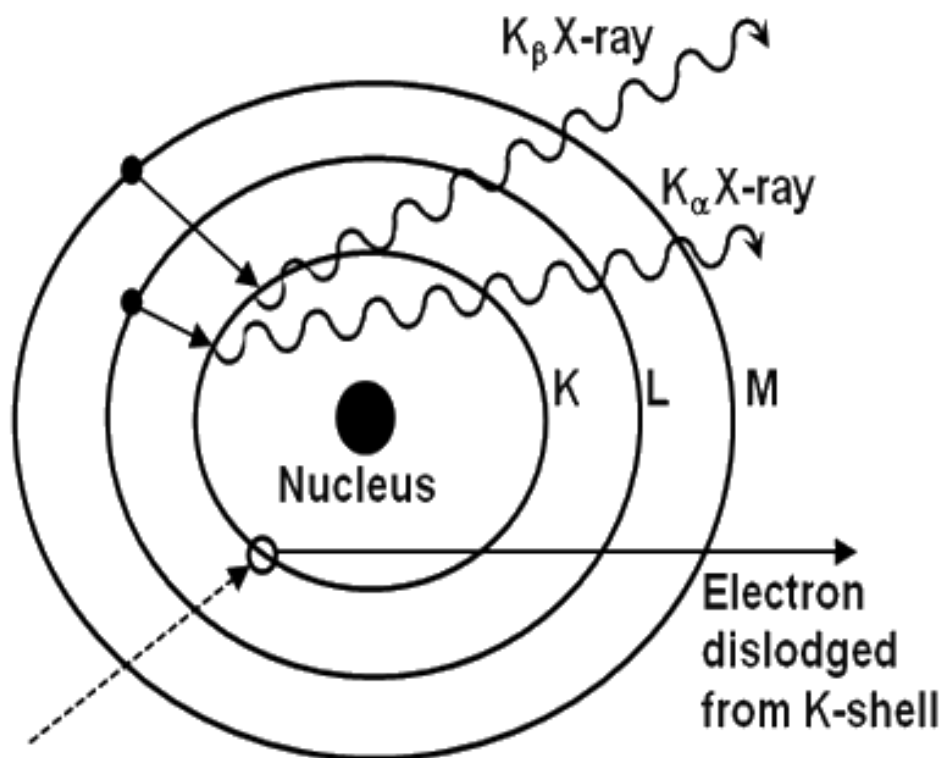
Figure 2.2. Generation of K-shell characteristic X-ray photons.

Bremsstrahlung radiation is caused by an incoming electron's trajectory approaching close to the nucleus of a target atom, and the difference in charge between the nucleus and the electron cause the energy and trajectory to be modified. In fact, the term Bremsstrahlung means "breaking radiation" in German, and the difference in the initial and final energy of the incoming electron is equal to the energy of the Bremsstrahlung X-ray photon. This explains why there is a continuum of Bremsstrahlung X-ray photons and not discrete energies for the case of characteristic X-rays. An example of a typical X-ray source, operating with a tungsten target at 100 kVp, is seen in Figure 2.3.[1], and the characteristic X-rays are seen as the spikes in X-ray output around 60 keV. The rest of the energy spectrum is a direct result from primary and secondary Bremsstrahlung interactions. The loss of low energy X-rays is not avoidable due to self-shielding effects and large absorption cross sections at low energies [11].
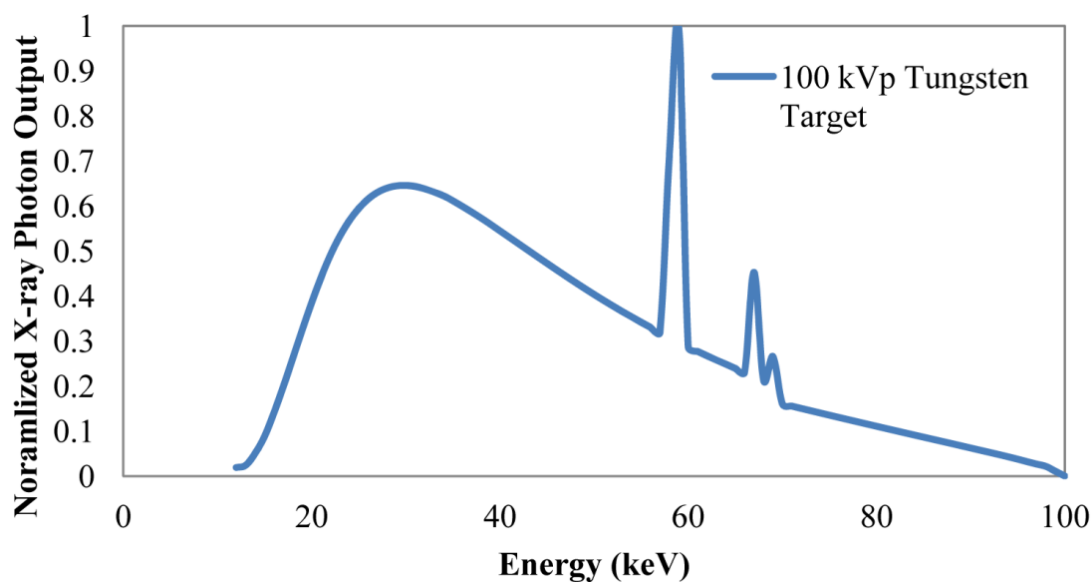
Figure 2.3. Typical X-ray energy spectrum operating at 100 kVp.

---

[1] Figure was generated using SpekCalc 1.1 using a tungsten target an anode angle of 30 degrees.

The overall geometry of the anode and target material will affect the X-ray energy spectrum. Different materials naturally have different characteristic X-ray photon energies, as seen in Table 1.1. The L and M electron shells also produce characteristic X-rays, but their energies are relatively low and most useable elements just do not have enough electrons to produce M-shell X-rays. In general, K-shell characteristic X-ray photons are the only useable photons unless special low energy resolution (10 keV to 1 keV energy resolution) X-ray detectors are used.

Table 1.1. Characteristic X-ray photon energy (keV) [11].

Element	$K_{\alpha 1}$	$K_{\alpha 2}$	$K_{\beta 1}$	$L_{\alpha 1}$	$L_{\alpha 2}$	$L_{\beta 1}$	$L_{\beta 2}$	$L_{\gamma 1}$	$M_{\alpha 1}$
W	59.318	57.918	67.244	8.398	8.335	9.672	9.961	11.285	1.775
Mo	14.479	17.343	19.608	2.293	2.289	2.394	2.518	2.623	N/A
Rh	20.216	20.073	22.723	2.696	2.692	2.834	3.001	3.148	N/A

2.1.3. X-Ray Filters and Collimators. Typical X-ray tubes use a variety of different filter and collimator designs. In general, traditional X-ray sources use two types of collimators and a single filter during operation, as seen in Figure 2.4. The first collimator/anti-scatter grid is generally integrated to the detector assembly to reject scattered photons at the image site. On the tube there is also a collimator, but this is just a collimator to shield/remove X-rays generated at large angles. Finally, the filter is also attached to the X-ray tube assembly to modify the X-ray energy spectra before passing through the imaged object.
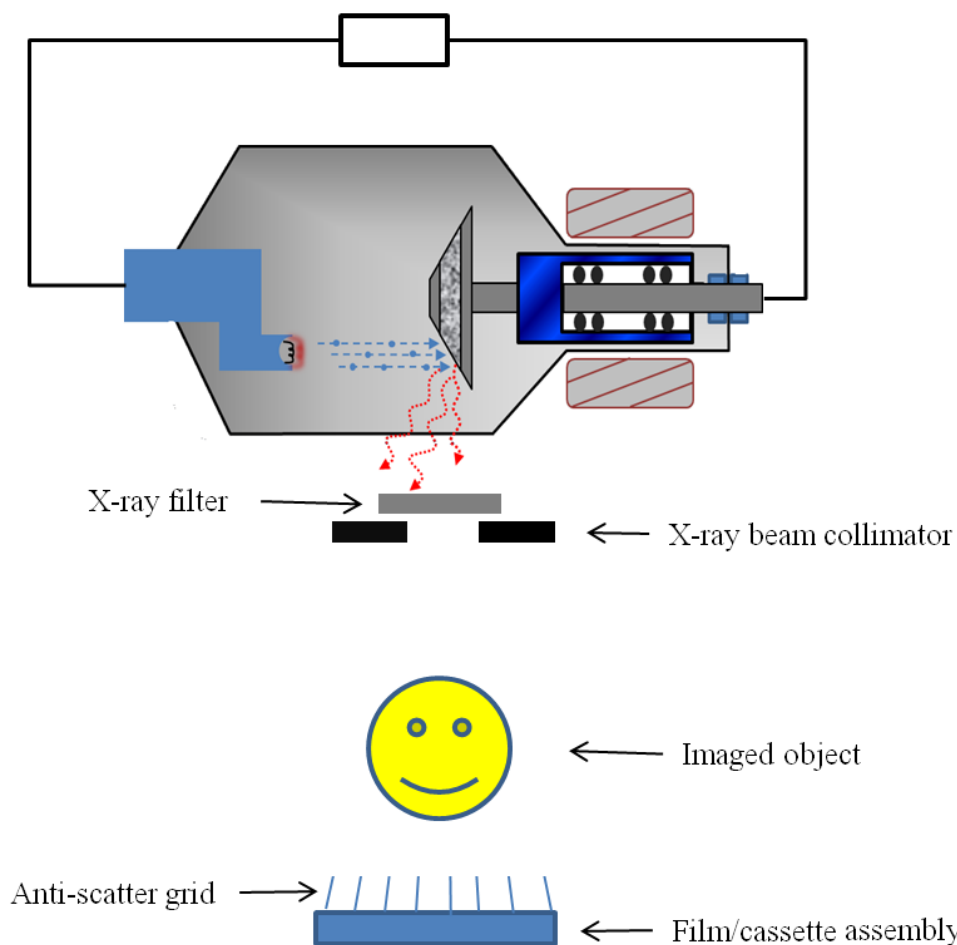
Figure 2.4. Typical film radiography setup with a traditional X-ray source.

Filtration is used to control the overall shape of the X-ray beam by removing lower energy X-rays. For medical physics applications, low atomic number materials, such as aluminum, are used for X-ray energy filtration. Furthermore, the removal of these low energy X-rays lowers the total dose to imaged patients. Figure 2.5 shows how the X-ray energy spectrum changes by introducing a 2.5 mm thin sheet of Aluminum. In fact, the average X-ray energy increased from 56.00 keV to 59.69 keV; just by filtering out some of the softer energy X-rays.
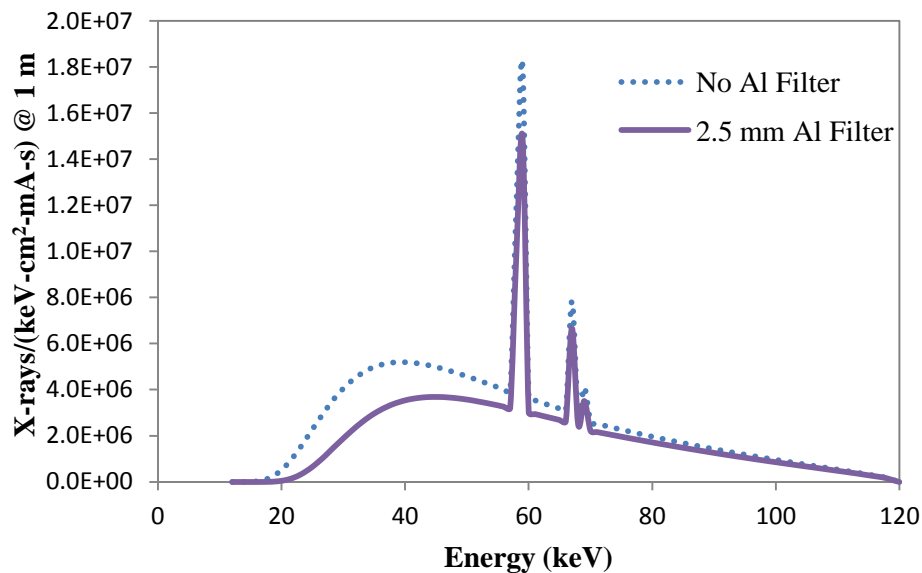
Figure 2.5. A 120 kVp traditional W anode X-ray source energy spectrum with and without aluminum filtration.

Also, different geometric shapes of filters change the radiation field, which is important for reflection type X-ray sources that intrinsically add a non-uniform radiation field via the heel effect, as seen in Figure 2.6. The heel effect is caused by angular beam hardening because the path length for the X-rays is a function of emission angle. Thus, the X-rays angled more towards the cathode experience maximum beam hardening and self-shielding, which leads the lower X-ray intensity. In order to correct for the heel effect digital radiography has correction algorithms, but standard film type radiography systems need to increase the source-to-image distance such that the emitted X-ray angle is narrower. By narrowing the emission angle the variation of X-ray intensity is decreased. One beneficial use of the heel effect involves mammography [12]. The X-ray tube is positioned such that the maximum X-ray intensity (cathode side) points towards the chest cavity and the anode side points to the nipple. Thus the overall shape of the heel effect matches well with shape of the breast.
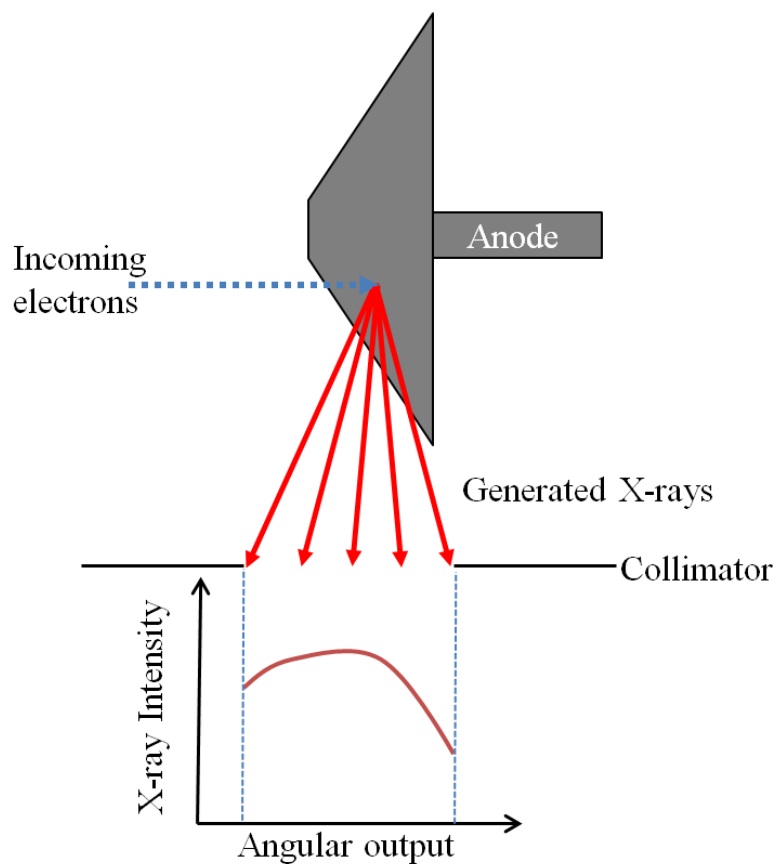
Figure 2.6. Heel effect with reflective type X-ray tubes.

2.2. COMPONENTS OF A FLAT-PANEL X-RAY SOURCE

While the operational nature of a flat-panel X-ray prototype mimics the operation of a traditional X-ray tube, the overall design is drastically different, as seen in Figure 2.7. Mainly, the flat-panel has a 2D array of individually controlled X-ray micro "tubes" or pixels, with respect to modern flat-panel displays.
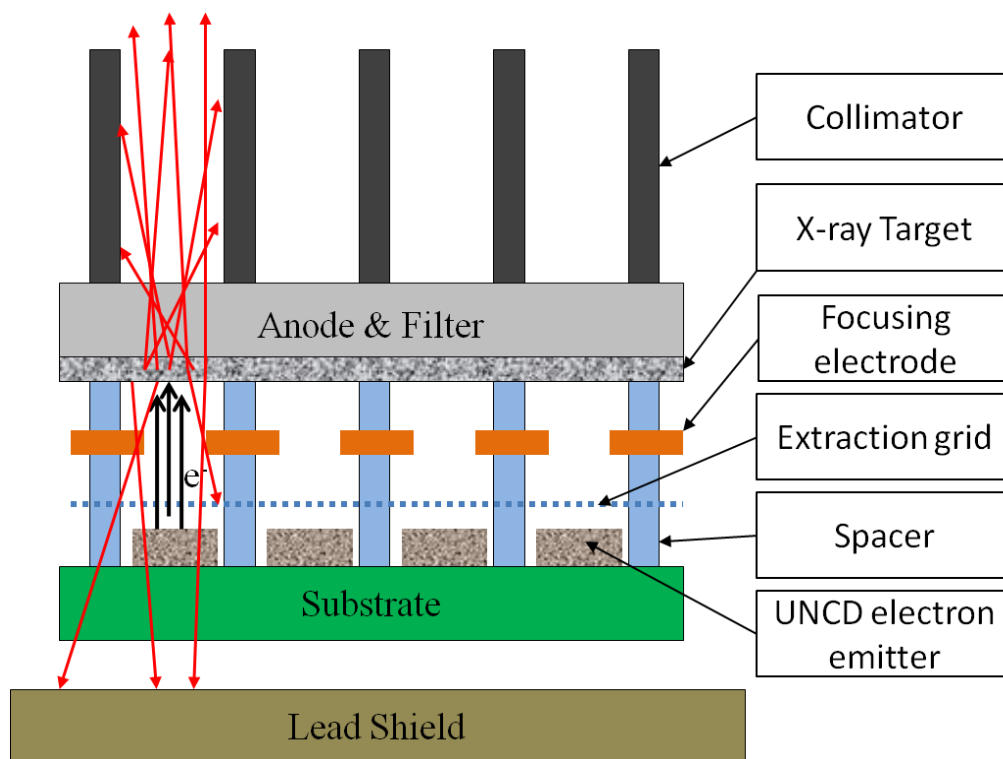
Figure 2.7. Cut away image of the flat-panel source.

With regards to a traditional X-ray tube, the focusing electrode, extraction grid, and UNCD electron emitter combine to form the "cathode assembly", but from there the overall design of the flat-panel X-ray source is dissimilar. Under an ultra high vacuum electrons are extracted via a low (< 1 kV) voltage bias between the UNCD emitters and the extraction grid. The gap between the UNCD and the electron extraction grid varies between several microns to tens of microns depending on the design of your cathode.   In fact, the emission current is directly proportional to the extraction grid bias.   The electrons are then accelerated towards the anode by another larger (> 30 kV) voltage bias, but during their trajectory the focusing electrode applies a static bias to converge the electron cloud, in the same manner as the focusing cup works with a conventional X-ray tube. The focusing electrode is positioned approximately several microns above the extraction grid to converge emitted electrons into a tight focal spot. The static bias at the focusing electrode controls final electron focal spot size at each individual pixel. Additionally, the distance between the cathode and anode is very important because, if

not selected correctly, voltage breakdown can occur and render the cathode useless. A good rule of thumb is, for every 10 kV you need the cathode to anode spacing should be 1 mm   Therefore, if operating with an electron accelerating voltage of 50 kV, the minimum spacing needs to be 5 mm (500 µm). Some of the key electron field emission components are detailed in Table 1.2.

Table 1.2. Key Electron Field Emission Variables.

Component	Variable	Dimension
Focusing electrode	Thickness and aperture	10 ~ 100 µm (thickness)
Extraction grid	Grid distance and aperture	20 ~ 100 µm (thickness)
Anode	Anode distance	500 ~ 5000 µm
Electrical parameters	Grid potential and duty cycle	Extraction potential, continuous or pulsed to prevent breakdown

Once the electron beam converges past the focusing electrode, the beam strikes the target, thus producing X-rays. With a transmission type X-ray, the target needs to be thin or self-shielding concerns arise, but the target also must be thick enough to generate a useful amount of X-rays. Furthermore, the operating kVp also changes the target thickness needed, as the linear attenuation coefficient is highly dependent upon energy. Our research shows, for 100 kVp or less, a tungsten target needs to 5 µm or less for optimal X-ray generation. Then, the X-rays travel into the filter which determines the final X-ray energy spectrum, depending on the application. The X-ray filter plays two key roles for our transmission X-ray source. First, the filter removes low energy X-rays, which lowers patient dose without affecting image quality and typical thicknesses for 100 kVp or lower operation is less than 2 mm of Al. Second, the material selected for the filter helps quickly conduct the high heat load generated within the target. Thus, making sure the tungsten target does not melt. Finally, the X-rays are then collimated by a micro fabricated metallic grid. The geometric design of a micro collimator is similar to that of

the X-ray filter as operating kVp can change the needed aspect ratio. For higher energy imaging, the septal thickness needs to increase for higher attenuation at a large angle which lowers the signal to noise ratio at the detector. Also, depending on the given task, a higher aspect ratio may be needed for higher resolution imaging. Some of the key X-ray generation components are detailed in Table 1.3.

Table 1.3. Key X-ray Emission Variables.

Component	Material	Dimension
X-ray target	Tungsten	0.5 ~ 5.0 µm thick
Anode and heat conductor	Aluminum or copper	0.25 ~ 2.0 mm thick
Collimator septa	Lead or tungsten	Aperture of 30 ~ 60 µm and height of 0.1 ~ 4.0 mm

2.2.1. Electron Generation. To improve upon the traditional X-ray source, our design utilizes the field emission phenomena over thermionic emission. The use of field emission has not gained much attention in terms of X-ray tube technology, besides the last decade or so. The biggest hurdle has been the fabrication of a stable field emission source of electrons, and the microfabrication techniques required did not exist until the last several decades [7,13-14]. The benefits of field emission are appealing when compared to thermionic emission such as lower power consumption and higher brightness [15]. Additionally, there are several different designs and materials used in cold cathodes, ranging from the original Spindt type emitters with molybdenum pyramidal tips to gated tips [4]. Furthermore, cold cathodes made from carbon based materials like carbon nanotubes (CNT) and diamond have been heavily researched [16-25]. However, the Nanofabrication & Devices group at Argonne National Laboratory first reported good field emission properties from UNCD even with planar geometry, without the need for coating them onto high aspect ratio tips, which simplifies the microfabrication process [26]. Furthermore, there is no need for externally heating the cathode, as the electron emission is controlled by electric fields. By controlling the electron emission using electric fields, there is no need to wait for the cathode to heat up, and in doing so, allows for quick electron pulses. Therefore, the prototype can be used as a fast pulsing source. In fact, due to their low power and fast pulsing capabilities, cold cathodes have been considered for microscale electric propulsion systems for spacecrafts [27].

The governing equation for electron field emission is called Fowler-Nordheim [28] and is seen in equation 2,

$$I = \frac{A_{FN}(\beta E)^2 A}{\Phi_{N-UNCD}} \exp\left(\frac{-B_{FN}v(y)\Phi_{N-UNCD}^{3/2}}{\beta E}\right) \tag{2}$$

where I is the emitted current collected at the gate from a field emission area A in m^2, E is the effective electric field acting over the emitting surface in V/m, β_{FN} is the characteristic field enhancement factor of the emitting surface, Φ_{N-UNCD} corresponds to the work function characteristics of the emitting material in eV, A$_{FN}$ is equal to1.5415 x

10^{-6} (A eV V^{-2}) and B$_{FN}$ is equal to 6.830 x 10^9 (eV$^{-3/2}$ V m^{-1}). The parameter $v(y)$ within the exponential term in equation 2 is set to 1 for carbon based emitters [8]. The reduction of the potential energy barrier needed for an electron to escape the emitting surface is shown as a function of the work function and the applied electric field, in Figure 2.8.
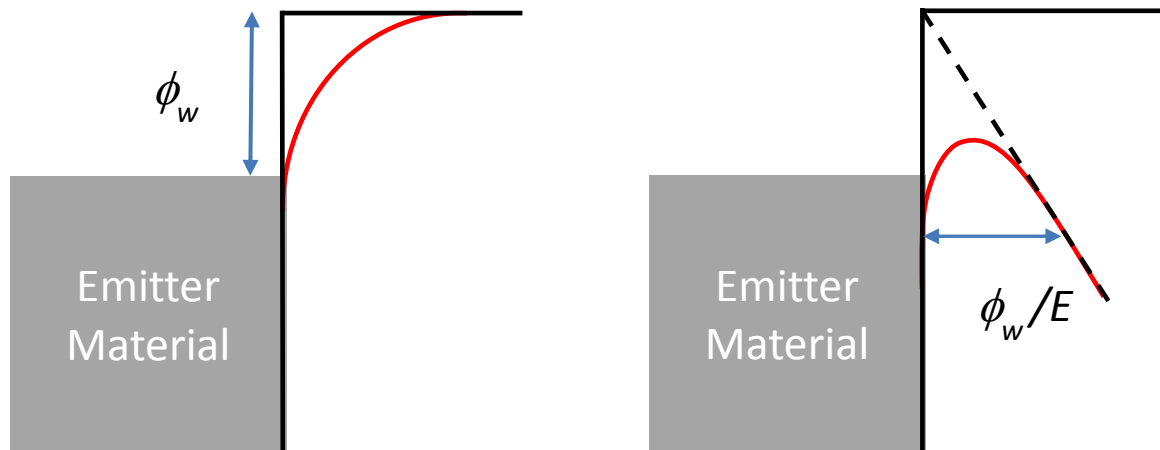
Figure 2.8. Potential energy barrier at the surface of the electron emitter A) no electric field B) with an applied electric field E.

2.2.2. X-Ray Generation. The physics behind X-ray generation within the flat-panel design is the same when compared to a conventional X-ray tube as explained earlier. However, the way they are utilized is completely different due to the fact that the flat-panel prototype uses a transmission type X-ray target and not the typical reflection type rotating anode assembly. A transmission target allows generated X-rays to easily pass through the anode; such that, the X-rays follow the same direction as the primary electron beam, as indicated by Figure 2.7. The electron interactions within the cathode material are what truly generate X-rays, as seen by Figure 2.9. Every red dot represents an electron interaction with the target, and can be highly computationally expensive for programs such as MCNPX.
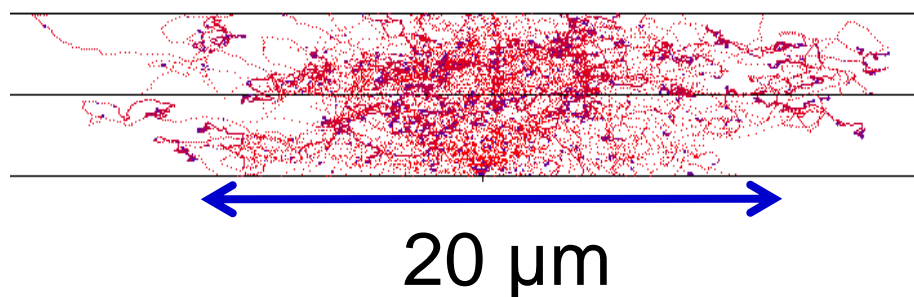
Figure 2.9. Monte Carlo simulation of electron interaction at anode.

A transmission type X-ray source yields several advantages, one example being a higher X-ray output per unit energy deposited by the electron beam. This is an advantage with our design as there is no need for active cooling [10]. Furthermore, since the design incorporates a large 2D plate as the anode/target, the heat distribution is far superior than a single focal spot. With better heat distribution, one area of interest is determining the maximum power at which the prototype may be operated without requiring active cooling. Previous work has indicated that the primary concern in transmission X-ray sources is the center of the electron beam at the incident target. Using a simple heat transfer equation, we have estimated the maximum operating power for a given electron focal spot size [29]. The analysis conservatively assumed the anode was made of aluminum 6061, which has a significantly lower melting temperature than tungsten. This assumption was made due to the fact that the tungsten layer can be sputtered (~600 nm) onto a thin aluminum 6061 plate, where the temperature will quickly conduct from the tungsten to the aluminum base. Furthermore, it was assumed that the initial electron beam radius would match half of the UNCD pixel area, which is 225 microns. Figure 2.10 shows that the centerline temperature on the anode will reach the melting point of aluminum 6061 if the prototype is operated at just over 45 W. Therefore, the prototype will be operated at less than 45 W during all testing operations.
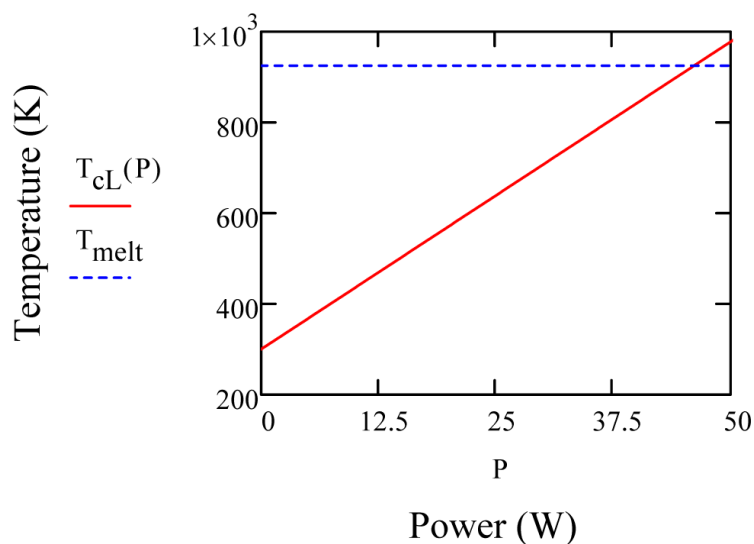
Figure 2.10. Maximum operational power level with respect to centerline anode temperature.

2.2.3. X-Ray Filters and Collimators. The transmission anode of our prototype allows for the combination of the X-ray source, X-ray filter and collimator to be integrated into one single unit. The X-ray filter and substrate material, shape and size will be selected to properly filter the X-ray energy spectra and placed onto the anode assembly. The selection of the filter material and thickness will be decided on application and energy range. For higher energy X-rays larger thicknesses will be needed for proper filtration. Also, low energies materials, such as beryllia, is used for its relative transparent attenuation with X-ray interactions. For our prototype, operating at 30 kVp, a simple 0.02" (0.5 mm) thick sheet of aluminum-6061 was selected. The thickness is large enough to cause good low energy filtration and helps dissipate heat from the anode, but future studies will look at optimizing filtration.

High aspect ratio micro collimator grids have been made available for X-ray imaging by Creatv MicroTech, as seen in Figure 2.11. Furthermore, they can be produced with a range of different metals with high X-ray attenuation coefficients such as Cu and Pb [30].
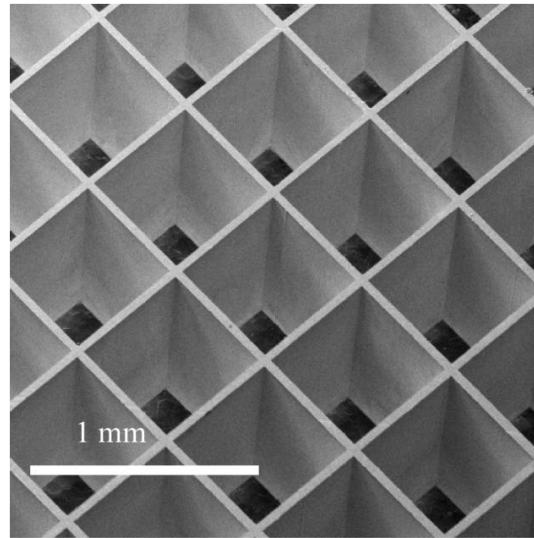
Figure 2.11. Micro fabricated anti scatter grid built by Creatv MicroTech [30].

To utilize our design for a parallel X-ray beam source a micro fabricated collimator much be used to allow for proper beam collimation, as shown above. Other benefits of using an integrated collimator allows for uniform radiation intensity from each micro X-ray source. Also, since the flat-panel X-ray source uses a transmission type anode there is no heel effect because the path length inside the X-ray target is identical for collimated transmission sources. Any X-rays that are generated at large angles are rejected by the micro collimator; therefore, again another reason why there is no need for a large source to object distance.

The collimation sizes, as described in Table 2-B, cannot be machined from a solid piece of material as there are no machining tools available at this scale and geometry. Therefore, they are fabricated using micro fabrication chemical and MEMS techniques.

3. MONTE CARLO SIMULATIONS

3.1. MONTE CARLO MCNPX MODELING

The Monte Carlo simulation code MCNPX 2.6.0 was used to simulate the interactions of the emitted electrons and generation of X-rays. MCNPX allows for many different physics options and energy treatments, which are highly important when building the model. The physics cards of both electrons and photons are equally important when modeling X-ray interactions with MCNPX. Generation and transport of secondary electrons was allowed in our simulation to account for Bremsstrahlung interactions as well as X-ray fluorescence. Coherent photon scattering and Doppler energy broadening for photons were also included; however, knock-on electrons were turned off during the modeling due to their large computational price, allowing us to decrease run times by a factor of 6-7. This setting is expected to not affect the accuracy of our results because the average energy of the knock-on electrons is only around ten percent of the peak voltage setting, and it is not high enough to create useful (high energy) X-rays for imaging. MCNPX simulations were run until all surface current tallies exhibited fractional standard deviations (relative error) less than 10 percent. A useful variance reduction technique, Bremsstrahlung biasing (BBREM), was applied to the high energy X-rays which are more important than lower energy photons in medical imaging. The benefits of using the BBREM card for Bremsstrahlung biasing is better sampling of the higher energy X-rays, including the important K-shell characteristic X-rays of tungsten. But, the downside is an increase in simulation run time due to higher energy electron-photon cascades [31].

For the backscatter electron results, the default method for the electron energy indexing algorithm needed to be changed on the DBCN card. The standard MCNPX algorithm uses "bin-centered" treatment between different electron energy groups as the Integrated Tiger Series (ITS) method uses "nearest group boundary" between different electron energy groups [31]. The standard algorithm yields artifacts in the backscattered electron energy spectrum due to its "bin-centered" treatment, but by using the ITS method the artifacts are removed [32-33].

The variables used in the investigation are shown in Figure 3.1. The energy of the incident electron beam on the target was assumed to be monochromatic based on our previous investigation of electron energy distributions [8].
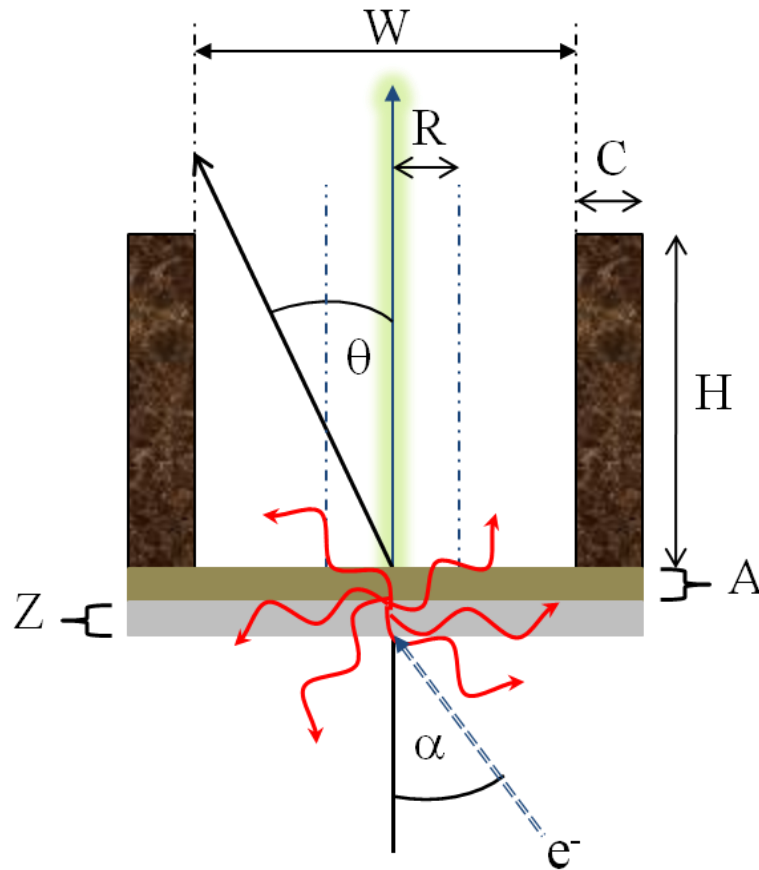
Figure 3.1. Targets with a thickness (Z) are hit using an electron beam of focal spot size (R) with an incident angle (α) in the MCNPX simulations. X-ray emission as a function of the polar angle (θ) was also investigated with collimation by septal thickness (C), height (H), and aperture width (W). The anode thickness (A) was held constant at 0.5 mm of aluminum and 0.5 mm of copper during the 30 kVp and 100 kVp simulations, respectively.

Two cases of the X-ray source were investigated to study the feasibility of applications to mammography and general radiography, as well as low and high energy imaging for NDE. Based on spatial resolutions and operation voltages of the current

mammography systems and digital radiography systems, an X-ray tube cell pitch of 50 μm and a tube voltage of 30 kVp were selected for mammography applications and 100 μm and 100 kVp for general radiography applications. The size of the focal spot (R), on which the electron beam is incident, is a function of the bias applied to the focusing electrodes and the voltage across the cathode and the grid. For this study, a focal spot size of 20 μm and 40 μm was selected for 50 μm and 100 μm cell pitch, respectively, based on our previous study of electron emissions [34].

Since only X-rays which have penetrated through the anode are used for imaging, the anode inherently acts as the X-ray filter. A suitable anode material would then be a material which has good electrical conductivity, good X-ray filtration capability, and good thermal conduction. Aluminum and copper would be suitable anode materials. Considering the attenuation characteristics of these metals, a 0.5 mm Al plate and a 0.5 mm Cu plate were selected as the anode of the 30 kVp and 100 kVp X-ray sources, respectively.

An X-ray transparent and electrically insulating material such as beryllia could be used to isolate the anode from the collimator; or, alternatively vacuum insulation would be suitable as well. In this study, the collimator was assumed to be in contact with the anode surface for simplicity.

3.2. X-RAY GENERATION

First, the X-ray energy spectrum of the proposed flat-panel X-ray source was compared with that of a conventional X-ray tube with the same conditions of anode voltage and filtration. For the calculation of the X-ray energy spectrum from the conventional X-ray tube, SpekCalc was used which is a semi-empirical program that models the energy spectrum of X-rays from conventional X-ray tubes [35]. Several limits of SpekCalc include X-ray energies ranging from 40 kVp to 300 kVp and anode angles between 6 degrees to 30 degrees [36]. The 100 kVp X-ray energy spectra from a flat-panel X-ray source and the conventional X-ray tube were normalized and compared in Figure 3.2.
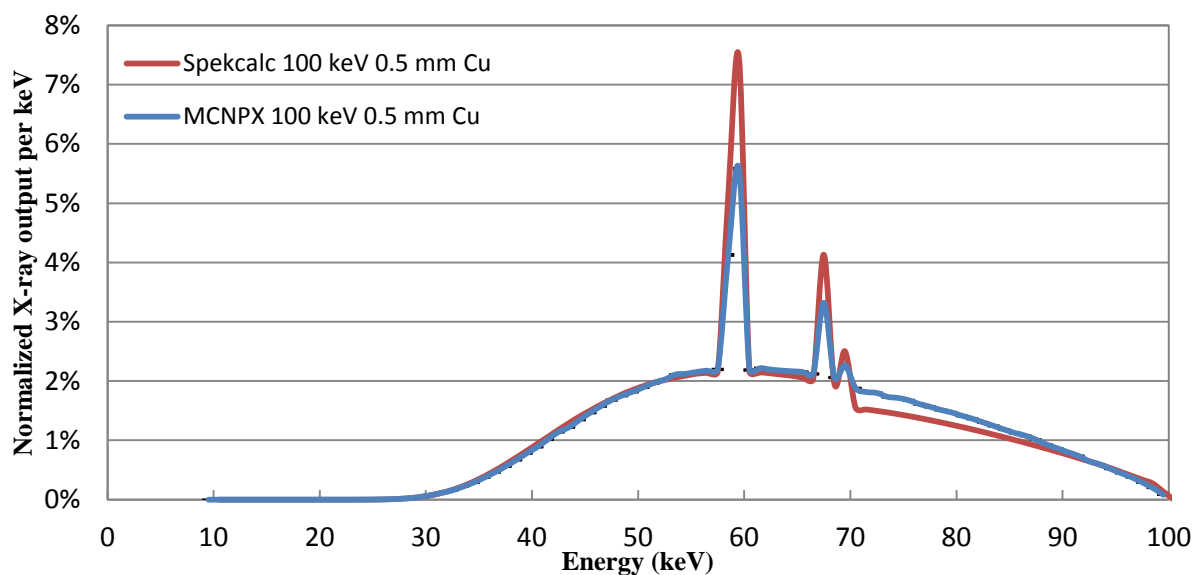
Figure 3.2. Comparison of X-ray energy spectra from MCNPX simulation of a flat-panel X-ray source versus SpekCalc calculation of a traditional X-ray tube. Both have identical anode voltage of 100 kV and 0.5 mm copper filtration but the anode used with SpekCalc was set at a 10 degree angle.

The 100 keV spectra, after passing through a 0.5 mm Cu filter, are similar. The 30 kVp spectra are not compared since the electron energy is lower than the bounds set by SpekCalc's useable range. The differences in the K-shell peaks can be attributed to the BBREM card use with MCNPX which bias the higher energy interactions. And also, the selected anode angle on SpekCalc affects the double differential cross section, which changes the amount of K-shell X-rays.

3.2.1. Target Optimization. When a beam of electrons strike the target, the electrons spread inside the target as they undergo many interactions. The spread is about 1 μm and 10 μm for 30 keV and 100 keV electrons, respectively. Thicker targets can produce more X-ray photons via more interactions per incident electron, but the escape probability of X-ray photons from inside the target diminishes. Figure 3.3 shows the effect of target thickness on the transmitted X-ray output from the target when it is bombarded with 30 keV and 100 keV electrons. The optimal thicknesses for the maximum X-ray output with a 30 keV electron beam were 1.0 μm, 1.25 μm, and 0.625 μm for rhodium, molybdenum, and tungsten, respectively. Among the three materials, tungsten produced the highest amount of transmitted X-ray intensity. The optimal thicknesses for the maximum output with a 100 keV electron beam were 7.0 μm, 9.0 μm, and 4.5 μm for rhodium, molybdenum, and tungsten, respectively, and again, tungsten is the best material for the maximum X-ray output.
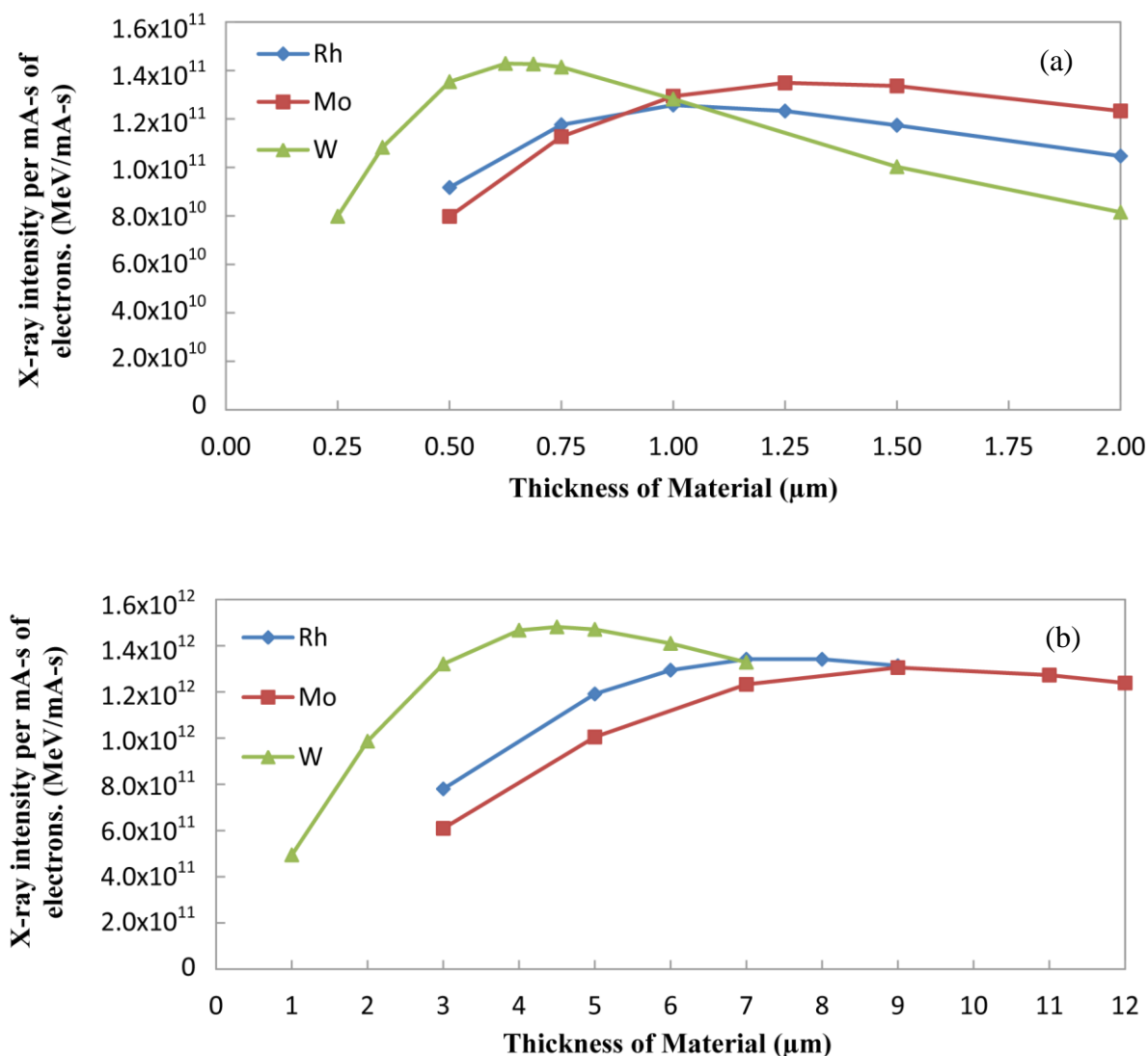
Figure 3.3. Target thickness effects on X-ray emission when Rh, Mo and W targets were bombarded with (a) 30 keV electrons and (b) 100 keV electrons.

3.2.2. X-ray Beam Intensity.   The energy spectra of the transmitted X-rays simulated with 30 keV and 100 keV electrons are shown in Figure 3.4.

The spectra were obtained with the optimal target thicknesses to produce the maximum X-ray intensity output. These results match well with previous research for tungsten and molybdenum targets [37]. In Figure 3.4 (a), tungsten shows a larger output in the 4 keV to 11 keV range, including its L-shell characteristic X-ray. Additionally, tungsten shows a larger total Bremsstrahlung tail past 11 keV. It is worth noting, from

Figure 3.4 (a), the K-shell peaks from Mo and Rh are large and contribute approximately 55% and 34% to the total intensity, respectively. This is why Mo and Rh are used as the target material in some of the X-ray tubes for mammography.
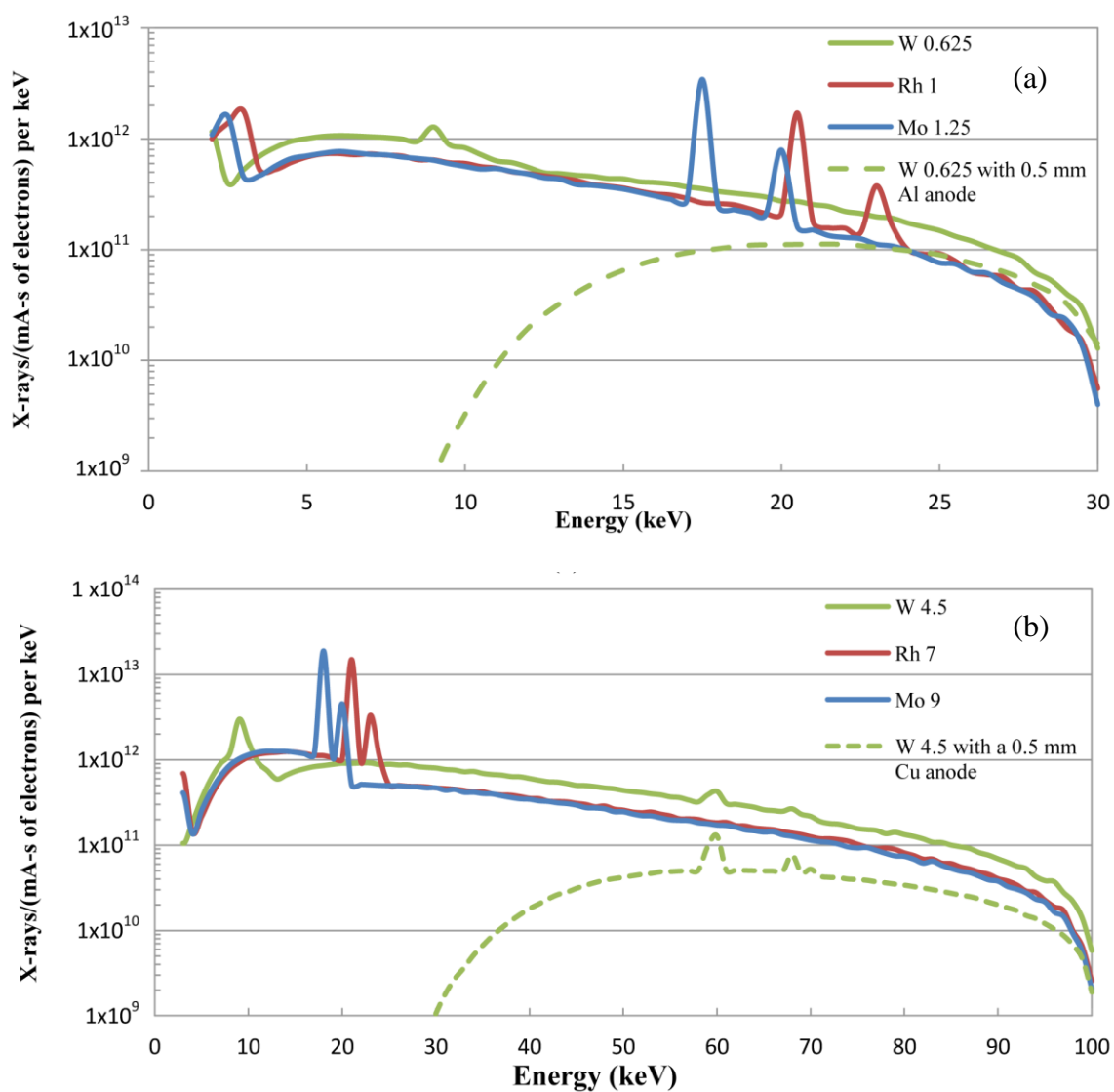
Figure 3.4. X-ray energy spectra from different target materials, (a) 30 kVp and (b) 100 kVp.

Furthermore, from Figure 3.4 (b) it is observed that the K-shell peaks from Mo and Rh are large and contribute approximately 32% and 27% to the total intensity,

respectively. Notice however, that these are occurring at the lower range of the energy spectrum. Below 22 keV, in Figure 3.4 (b), both Rh and Mo experience a larger X-ray output, if excluding the L-shell characteristic X-ray from W. But, low energy photons are usually filtered out to decrease the dose patients receive during imaging. Finally, tungsten shows a larger output for X-ray energies greater than 22 keV; thus, it is better than Mo or Rh for high energy X-ray imaging. Furthermore, the error bars were negligible and removed in Figure 3.4 for clarity, and the dashed line represents the X-ray energy spectra after passing through the tungsten target and 0.5 mm aluminum anode.

After passing through the anode, the low energy part of the X-ray energy spectrum has been reduced significantly, which is an additional function of the anode in our design. For clarity, only the optimum tungsten target thickness for both of the 30 kVp and 100 kVp cases are shown in Figure 3.4 with their anode attached.

In order to investigate the effect of electron beam direction on transmission X-ray output, the electron beam incident angle α was varied through a small angle ranging from 0 degrees to 19 degrees. The total X-ray output decreased by 3.3% for the 100 keV case and by 3.2% for the 30 keV case as the electron beam angle increased from 0 degrees to 19 degrees. Furthermore, as the electron beam angle increased from 0 degrees to 19 degrees, the intensity of re-emitted electrons increased by 4.0% for the 100 keV case and by 3.5% for the 30 keV case. For all incident angles, the X-ray output in the forward direction was higher than the opposite direction, as expected [38-39]. This indicates that transmission type X-ray sources, in principle, produce more X-rays compared to the reflection type X-ray sources with the same amount of X-ray tube current. As the incident angle α of the electron beam increases, the X-ray output decreases for both forward and backward directions. This loss of X-ray intensity is due to the fact that as the electron beam incident angle is increased, the fraction of the incident electrons that reemitted backwards from the target increases resulting in fewer amounts of electrons available for X-ray generation.

The transmitted X-rays show a slightly harder energy spectrum with respect to the backward X-rays as seen in Figure 3.5., which is another advantage over reflection type X-ray source when imaging thick samples or objects. The backward X-ray energy

spectrum would be useful for the calculation and design of shielding behind the cathode structure, but it's completely irrelevant for transmission X-ray imaging purposes.
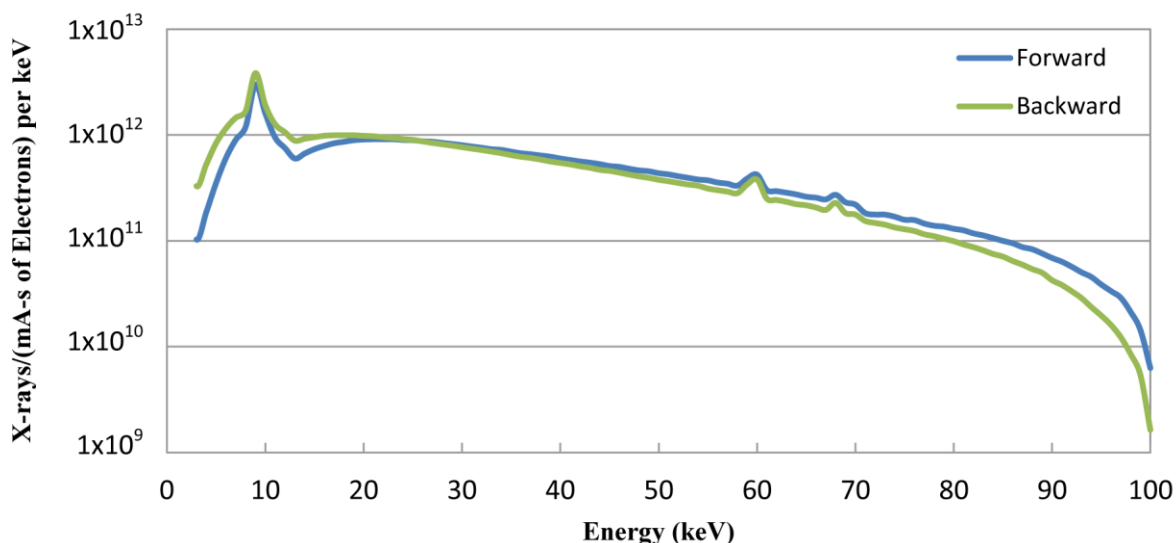
Figure 3.5. Energy spectra of forward and backward X-rays from a 4.5 μm thick tungsten target, normalized per mA-s packet of a100 keV e⁻ beam (error bars removed for clarity, but negligible).

3.2.3. Angular Distribution. An important feature of our design is the ability to generate a pencil beam of X-rays in the purely forward direction. For example, a transmitted beam with less than 1 degree of divergence yields a solid angle of less than 9.57×10^{-3} sr. The use of a high aspect ratio X-ray collimator would allow for narrow X-ray pencil beams with divergence of less than 1 degree. For proper design of a collimator, information of angular distribution of the X-rays from the target is needed. It is well known that with non-relativistic electrons (like the ones used here) the angular distribution of transmitted X-rays is broad and highly anisotropic [40]. The angular distribution of the X-ray output per unit solid angle obtained from the simulation study is plotted in Figure 3.6 as a function of the polar angle θ which was defined in Figure 3.1.
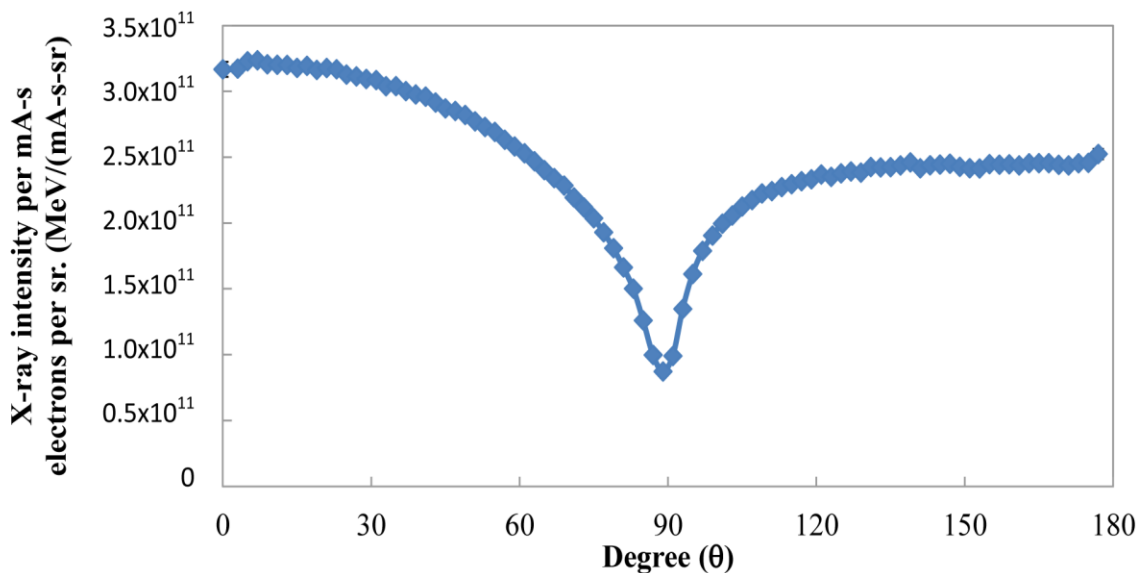
Figure 3.6. X-ray intensity per unit solid angle as a function of the polar angle θ. X-rays were generated from a 4.5 µm thick tungsten target hit by a 100 keV e⁻ beam. The forward direction is when θ = 0˚.

The error bars are higher near the poles (0˚ and 180˚), due to the smaller solid angle of intensity measurement in those regions, i.e. smaller sampling space. It is shown that the X-ray intensity per solid angle is highest in the forward direction (θ = 0˚, 3.22 $\times 10^{11}$ MeV/mA-s-sr.); and, in fact, is more than 30 percent higher than the opposite direction (θ = 180˚). Therefore, coupling this flat-panel X-ray source to a parallel-hole collimator can indeed produce adequate parallel pencil beams for imaging purposes.

3.2.4. Backscattered Electrons. From the simulation study, we could observe that a significant amount of electrons were re-emitted from the target in the opposite direction to the incident electron beam direction. Figure 3.7 shows the energy spectrum of the re-emitted electrons for the case of 100 keV electron beam incident on a W target. It is shown that most of the re-emitted electrons have high energies. Tavora et al. also showed that a large portion of primary electrons were re-emitted toward the cathode when they were incident on a silver target [41]. These re-emitted electrons can affect the electric field driving the primary electrons and affect the performance of the device. If enough electrons are scattered towards the cathode, they can effectively shield the high electric field by creating a virtual cathode [42-43]. Also, once a virtual cathode is created, the electron emission rate transitions from a continuous to an oscillatory emission [44]. The loss of useable primary electrons is undesirable because it decreases the overall efficiency of the X-ray source. Further research is required to solve the introduction of a virtual cathode which limits the emission of primary electrons due to the physical phenomena of space-charge buildup.
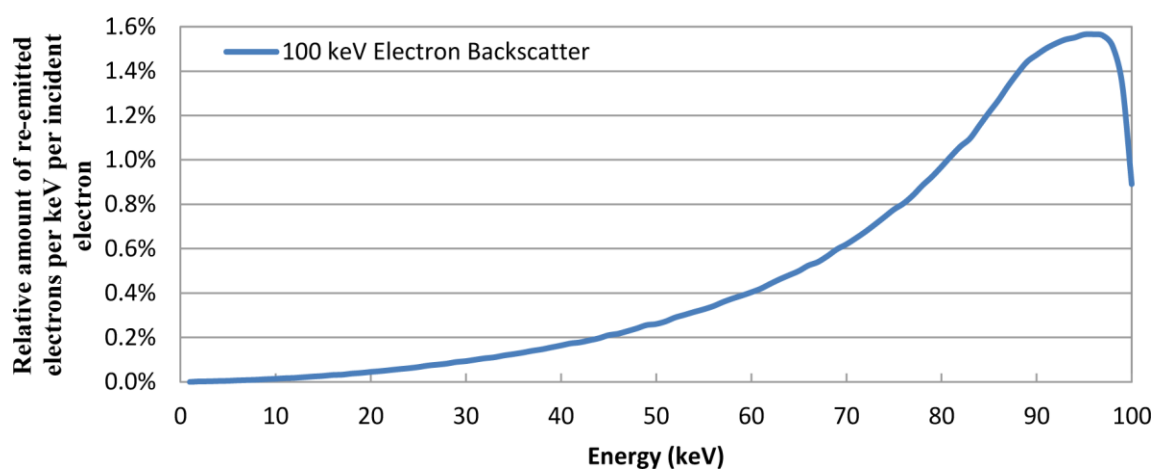
Figure 3.7. Energy spectrum of the re-emitted electrons in the backward direction from a 4.5 µm W target when 100 keV electrons bombarded it.

3.3. X-RAY COLLIMATION

The collimator serves as a way to passively create narrow X-ray pencil beams. Current anti-scatter grid and micro-collimator technology allows for septal thicknesses tens of microns thick with aspect ratios greater than 100 [30]. The size of the grid is limited by the mask used during the lithography process; therefore, the larger the mask, the larger the collimation grid can be made. For the simulations, tungsten collimators with aspect ratios ranging from 75 to 125 were tested. Another important consideration is that the septa of the collimator must not cross over the focal spot in an X-ray tube cell; therefore, the septal thickness is limited both by the cell pitch and the focal spot size.

The effectiveness of the collimator is shown in Figure 3.8., where the relative X-ray intensities emitted from neighboring collimator openings are compared with that of the operating cell located at the center. The nomenclature of AR100-S60 is equal to an aspect ratio of 100 and septal thickness of 60 μm, and results are normalized to the output from the operating center pixel. The results show that the intensity from the closest neighboring collimator opening drops to less than 1% of the intensity from the operating cell. The efficiency of the collimator is obviously affected by its geometry, as in the case of anti-scatter grids in X-ray imaging.
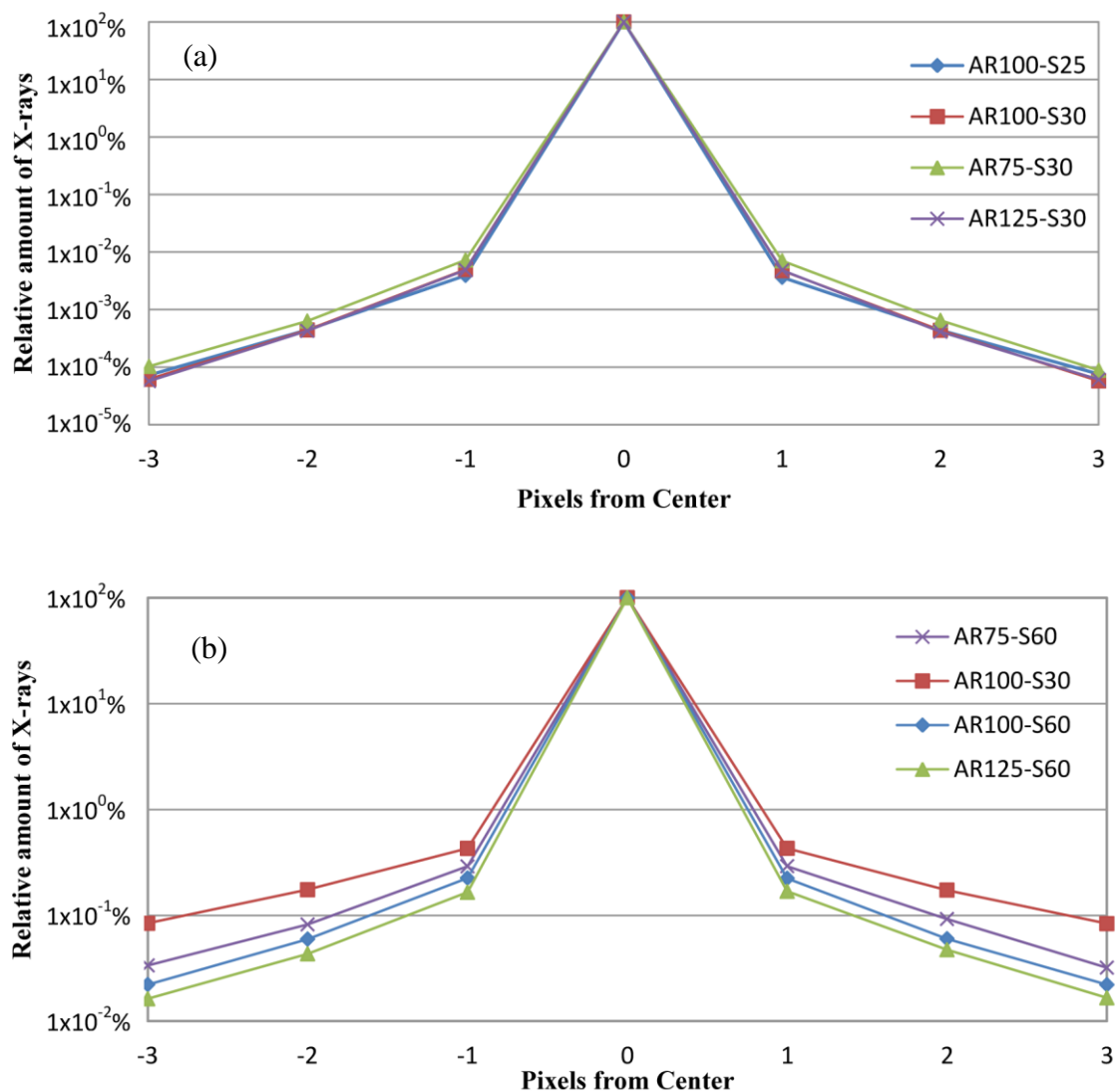
Figure 3.8. Collimated X-ray intensities from neighboring X-ray tube cells, (a) from 0.625 μm W target, 0.5 mm Al anode and 50 μm cell pitch at 30 kVp, and (b) from 4.5 μm W target, 0.5 mm Cu anode and 100 μm cell pitch at 100 kVp.

In Figure 3.8 it is shown that as the collimation efficiency raises, i.e. the intensities from the neighboring opening drop, while the aspect ratio of the collimator increases. It can also be seen that with the same aspect ratio, a collimator with thicker septa shows better collimation efficiency, due to more material blocking X-rays directed to the neighboring collimator holes. The aspect ratio was defined as the ratio of the collimator height (H) and width between the inside walls of the collimator (W), as shown

in Figure 3.1. From Figure 3.8 (a), it can be said, due to tungsten's almost perfect absorption of low energy X-rays, that collimator efficiency is not affected by aspect ratio when the septal thickness is large enough. Additionally, the septal thickness described in Figure 10 is equal to two times the collimator thickness (C) because the total thickness is shared between two bordering pixels.

Increasing the aspect ratio, however, reduces the X-ray intensity from the operating cell. The final X-ray intensity from a 100 kVp tube cell, after passing through a collimator, is plotted in Figure 3.9 as a function of the aspect ratio at various septal thicknesses. A collimator hole with a higher aspect ratio has a lower solid angle, permitting less X-ray photons to travel past the collimator without interacting with the septa. This effect is clearly shown in Figure 3.9.
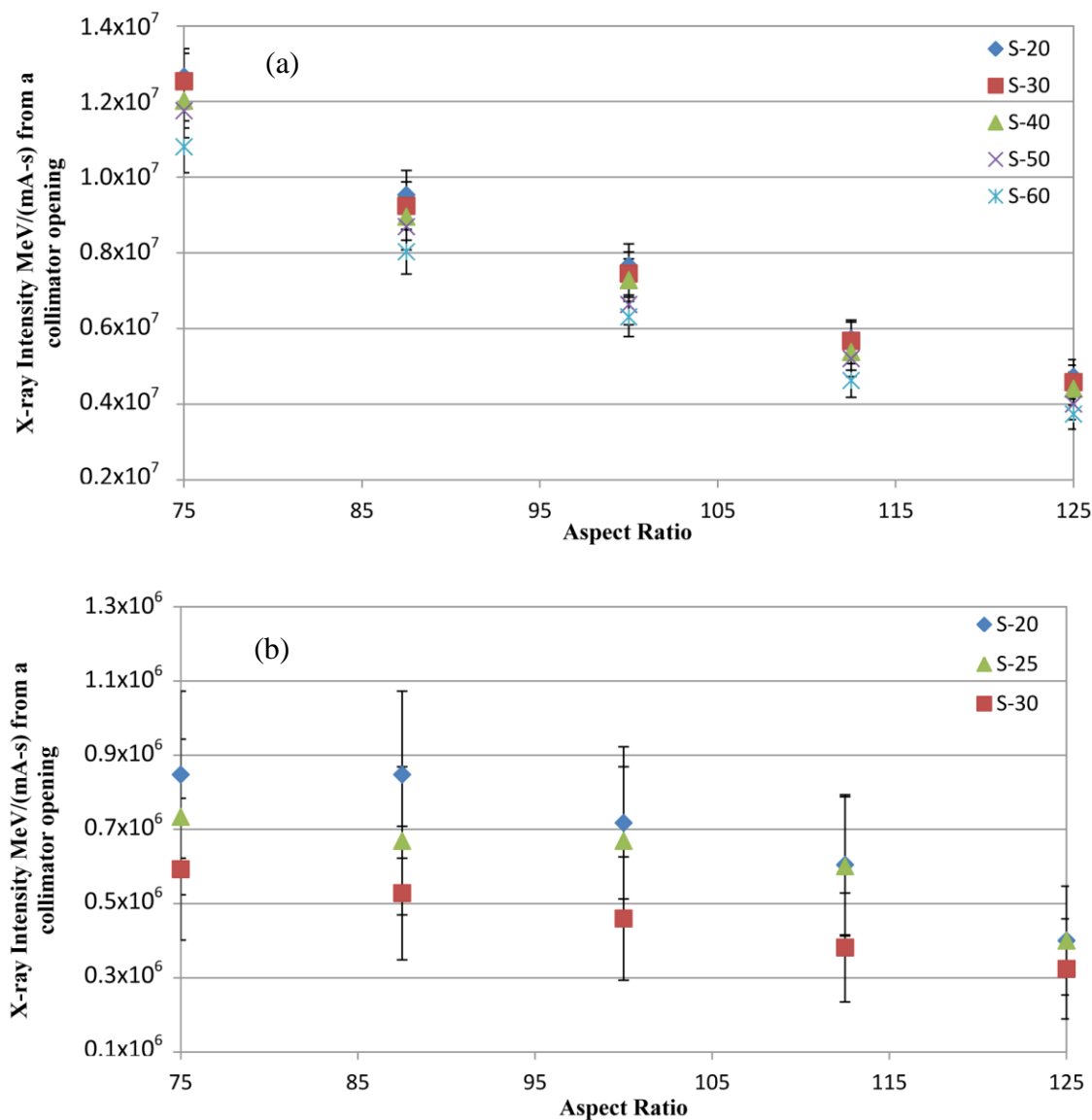
Figure 3.9. X-ray intensity from a collimator opening as a function of the collimator aspect ratio. Simulation condition: (a) 100 keV electrons, 40 μm focal spot, 4.5 μm W target and 0.5 mm Cu anode and (b) 30 keV electrons, 20 μm focal spot, 0.625 μm W target and 0.5 mm Al anode (the legend nomenclature is S for the septal thickness followed by the thickness in μm).

It can also be seen in the figure above that, for a given aspect ratio, the X-ray intensity is slightly reduced with a thicker septa, which is due to reduced size of the collimator opening while the size of the focal spot remains the same. The error bars in Figure 3.9. (b) are higher than 10 percent, but even running the maximum amount of

particles allowed in MCNPX did not help reduce the error. The large error is attributed to the small cell size of the 30 keV pixels, which translate to a smaller sample space and therefore higher statistical error.

From the results it is possible to directly compare the output from a traditional X-ray source to our new flat-panel X-ray prototype. In order to compare the two units, the X-ray intensity passing directly in front of each source was measured. To simulate a standard flat-panel X-ray detector, an area of 0.001 cm^2 was selected to measure the X-rays. For the traditional X-ray source, the area of interest was positioned 60 cm away, which is a typical distance in X-ray imaging. The flat-panel prototype had the area of interest 10 cm away, which is feasible since the source produces parallel beams of X-rays. As seen in Table 3.1, the flat-panel X-ray source intensity per detector pixel is approximately 300 times higher than a traditional X-ray source.

Table 3.1. Comparison of flat-panel and conventional X-ray Sources.

Source	Intensity (MeV/(mA-cm^2-s))	Detector pixel size (cm^2)	Distance from source	Intensity at the pixel (MeV/(mA-s)
Conventional	$1.87 \cdot 10^5$	0.0001	60 cm	18.7
Flat-panel*	$5.93 \cdot 10^9$	0.0001	10 cm	$5.93 \cdot 10^3$ **(~300 times higher)**

* MCNPX calculation is for S-30 Aspect Ratio 75 case in Figure 3.9

4. PROTOTYPE FABRICATION AND OPRERATION

4.1. VACUUM AND HIGH VOLTAGE SYSTEM DESIGN

In order to properly test the flat-panel X-ray source, a vacuum chamber was needed for generating electrons. A spherical vacuum chamber with multiple flange inlets was connected to a turbomolecular pump, which reduces the system to 10^{-9} torr, and a rotary vane pump, which serves as a roughing pump that lowers the pressure before the turbo pump is started, as seen in Figure 4.1. The vacuum system is fully constructed and has an operational pressure of $2 \cdot 10^{-8}$ Torr. The operating pressure was higher than expected, but the use of a rubber gasket on a viewport limits the chamber from reaching lower pressures. However, the operational pressure was deemed enough for our field emission testing. Other connections to the vacuum chamber include: a 60 kV electrical feedthrough, a 30 kV electrical feedthrough, a 500 V electrical feedthrough, a 2.75 inch diameter beryllium window, a micropositioners, a 6 inch standard viewport and a residual gas analyzer (RGA).
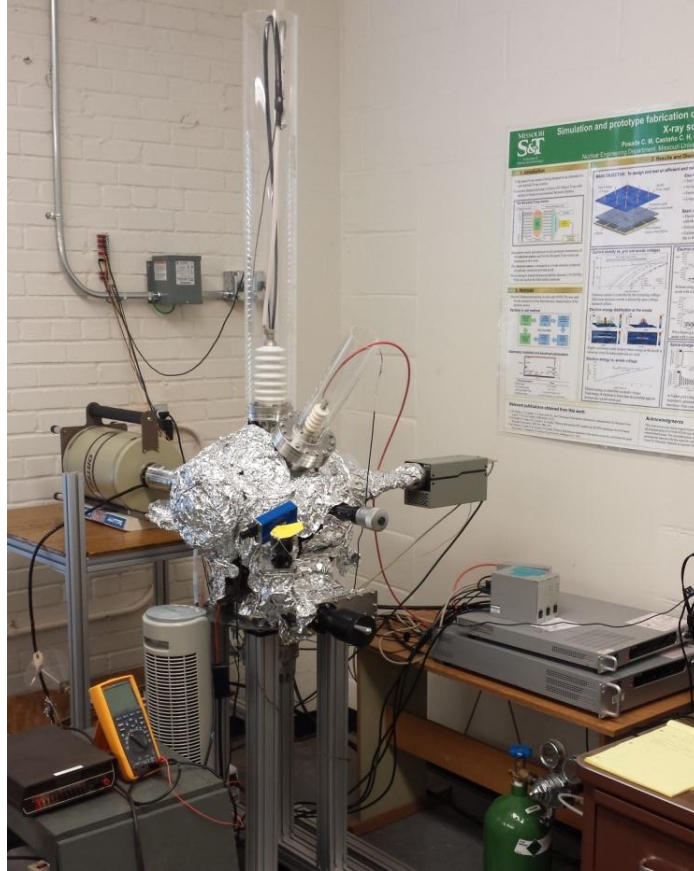
Figure 4.1. High vacuum system for prototype testing.

The three separate electrical feedthroughs are needed for electric extraction, electron beam focusing and electron acceleration. The 60 kV voltage feedthrough was selected for electron acceleration to the anode. Proper connections between feedthrough, power supply, and external ground were guaranteed before use of the high voltage system. The 30 kV feedthrough was used for an electron source that was purchased for a comparison between our design and a commercially available field emission source. Finally the low voltage feedthrough was used for voltage bias between the UNCD and electron extraction grid, and it can be used as a way to power a focusing lens to control the electron beam spot size.

The thin beryllium window is used for its low X-ray attenuation properties. However, for initial testing, the 6" viewport was used due to geometric issues with the spherical vacuum chamber. The viewport is hinged such that, if something needs to be

changed within the vacuum chamber, the port can be opened by just unscrewing a single holding bolt. This makes it much easier than needing to unbolt the whole flange and replace a copper gasket just to make simple changes to the system. After opening the system, the RGA was used to verify that there were no new leaks in the system and to verify that the newly inserted materials were not offgassing. Offgassing is a major concern due to the fact that it could increase the pressure inside the chamber, and these molecules could cause electrical breakdown due to the high electric fields generated from the high voltage power supply.

The selection of the power supplies matched with the selections of electrical feedthroughs for the vacuum system. However, there was one major criterion which limited the possible selections which was that all of the power supplies must be PC controlled. By having the power supplies computer controlled, no one is needed to stand near the X-ray source during operation. This insures that no one receives unneeded X-ray dose and practices proper radiation safety.

With the previous simulation and heat transfer work, the needed voltage and amperage were known for the new power supplies. The prototype flat-panel X-ray source was built to produce 30 kVp X-rays, but future plans include expanding its capability to utilize 100 kVp X-rays. Therefore, a 120 kVp 10 mA power supply was selected for accelerating the generated electrons to the X-ray target. Having 10 mA allows experimental testing well below the maximum operating power before melting the anode, but also will yield more than enough X-rays for measurement purposes. For the UNCD and electron extraction circuit, a separate 650 V 100 mA power supply was selected which allows for electric fields greater than 20 volts per micron. A different 5 kV 20 mA power supply was selected for the commercial field emission source since the source operates at a much higher voltage (greater than 2000 V). Figure 4.2 shows the power supply set up used for experimentation.

Figure 4.2. Power supplies used for electron extraction and acceleration. (A) Computer control interface, (B) 5 kV power supply, (C) 120 kV power supply.

4.2. CATHODE CONSTRUCTION

The prototype cathode was monolithically fabricated using micro fabrication techniques. The flow schematic is shown in Figure 4.3. We used p type (100) Si wafers coated with a low stress one micron Si_3N_4 deposited by low-pressure chemical vapor deposition (LPCVD). The Si_3N_4 is necessary for electrical insulation (you could add more details). A thin layer of tungsten (250 nm) is sputtered onto the Si3N4 layer for an electrical connection to the N-UNCD emitters and as a good seed layer for the N-UNCD growth[22].
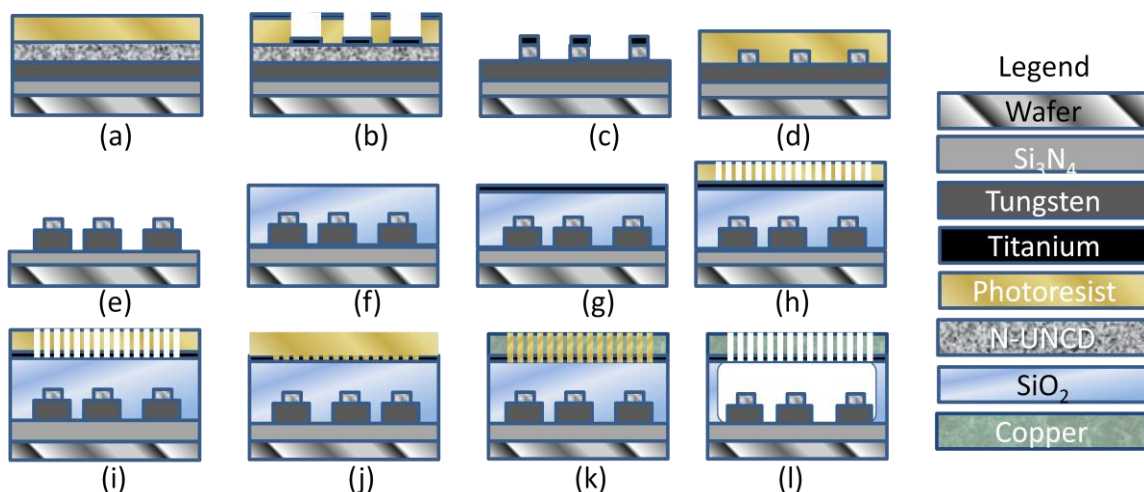
Figure 4.3. Micro fabrication flow chart: (a) layering of wafer, Si3N4, tungsten, N-UNCD and photoresist (b) UV lithography mask 1 and Ti mask (c) PR removal and N-UNCD etch (d) Ti mask removal and PR addition for tungsten etch (e) UV lithography mask 2 and tungsten etch (f) 5 microns of SiO2 for electrical insulation (g) tungsten seed layer for copper electroplating (h) PR addition and UV mask 3 lithography for W seed layer etch (i) negative PR UV lithography mask 3 (k) electroplate copper and use negative PR as growth guide (l) BOE etch of SiO2 under W copper grid for field emission.

The metal deposition was done using a magnetron sputtering system (AJA International Inc.) or by using a Lesker PVD-250 electron-beam evaporator with a Sigma deposition controller at a base pressure of 10^{-8} Torr. Tungsten was selected for its ability to withstand the high temperatures (850°C) encountered in the microwave plasma assisted chemical vapor deposition (MPCVD) used during the N-UNCD growth (915 MHz large-area MPCVD system – Lambda Technologies Inc.). To obtain a hard mask for pattern transfer in N-UNCD, a 50 nm Titanium layer was deposited by e-beam evaporation after UV lithography. For patterning we used 2.7-μm-thick S1827 (Shipley) photoresist spin coated at 3000 rpm, baked at 115^0C for 1 min and exposed using a Karl Suss MA-6 mask aligner. The pattern was developed in 351 Microposit developer diluted 1:3 in deionized water (DIW) for 20 s. Lift-off of the Ti was done at 100^0C in 1165 Remover for 3 hours, and an ultrasonic agitation was used for 90 s at the end of this step. The N-UNCD layer was etched by ICP-RIE PlasmaLab 100, using oxygen 50 sccm (sccm denotes standard cubic centimeter per minute at standard temperature and pressure,

STP), chamber pressure 10 mTorr, 1200 W ICP power and 10W RF power (etching rate ~50 nm min-1) [23]. After the N-UNCD etch, the hard mask was removed with a solution of HF and H2O, ratio 1:9.

The next step was to create the tungsten electrical wiring circuit, which required another UV optical lithography, using a negative photoresist maN-415 (Microchem), spun at 3000 rpm and baked for 90 s at 100°C to get a thickness of 1.5 μm. , The tungsten was etched by RIE (CS 1700 March) with SF_6 20 sccm, chamber pressure 150 mTorr, RF power 250W, etching rate ~80 nm min-1. After etching the photoresist was removed with acetone. The tungsten wiring circuit is showed in Figure 4.4.
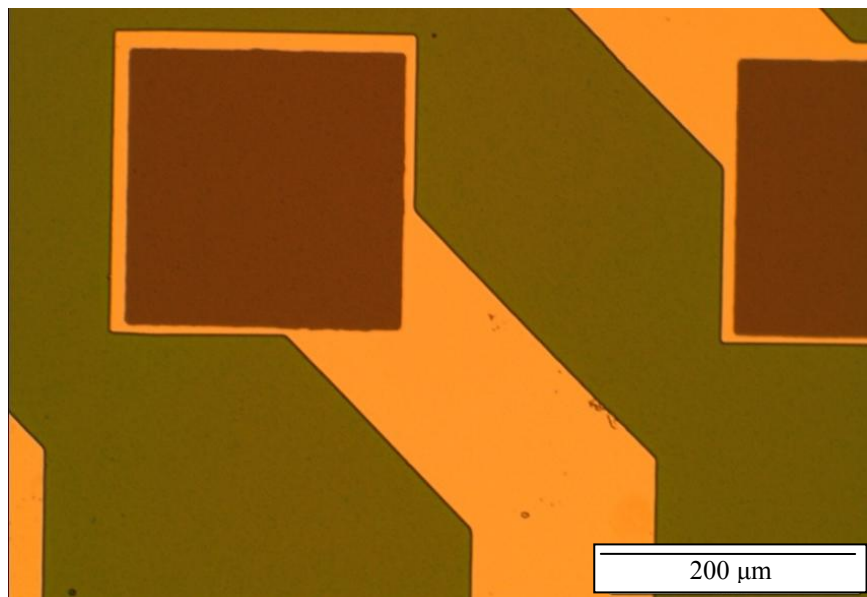
Figure 4.4. Micro fabricated tungsten voltage lines (yellow) with N-UNCD electron emitters aligned upon them (rust). The tungsten was sputtered upon the Si_3N_4 insulating layer (green). Legend in bottom right states 200 microns.

Once the tungsten wiring scheme is complete, the base cathode fabrication is complete. In order to integrate the electron extraction grid, a standoff and electrically insulating layer is needed. A layer of SiO_2 was selected due to its high dielectric strength and was deposited by plasma enhanced chemical vapor deposition PECVD, at low

temperature $100^{o}C$ (ICP CVD Oxford) for a thickness greater than one micron. During fabrication, a limit of five microns was selected due to the fact that deposited SiO_2 on the chamber walls started to flake off and contaminate the wafer surface.

Copper was chosen as the electron extraction grid material due to its desirable electrical and thermal properties. In order to electroplate copper a thin 50 nm layer of W as base plating was first sputtered onto the SiO_2 surface. By using a third UV optical lithography, with a positive photoresist S-1818, the location of copper electroplating was controlled, thus allowing for a thickness of 1.8 µm copper grid with small electron extraction openings as seen in Figure 4.5.

200 µm
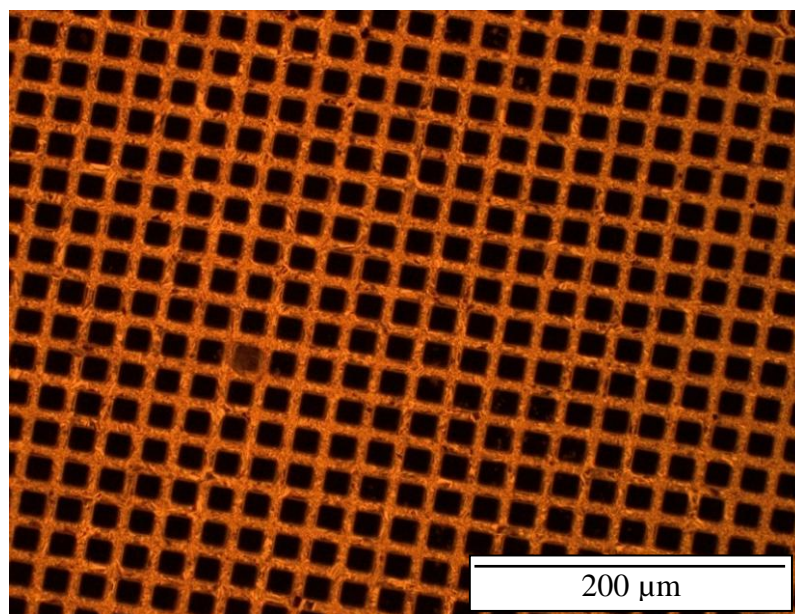
Figure 4.5. Dark field image of the electron extraction grid with dimensions of a pitch of 25 µm, hole-width of 19 µm and connecting bar thickness of 6 µm.

The copper electroplating was performed using a copper sulfate plating process from Lea Ronal, Inc. An acetone bath was used to strip the photoresist from the surface. Another quick SF_6 RIE was used to remove the tungsten base plate layer where the grid holes were left from the removal of the photoresist. As a result, the wafer was ready for

the final SiO_2 etch step to expose the N-UNCDs under the grid. A buffered oxide etchant (BOE) was used to etch the SiO_2 layer and create a free membrane/grid as seen in Figure 4.6.
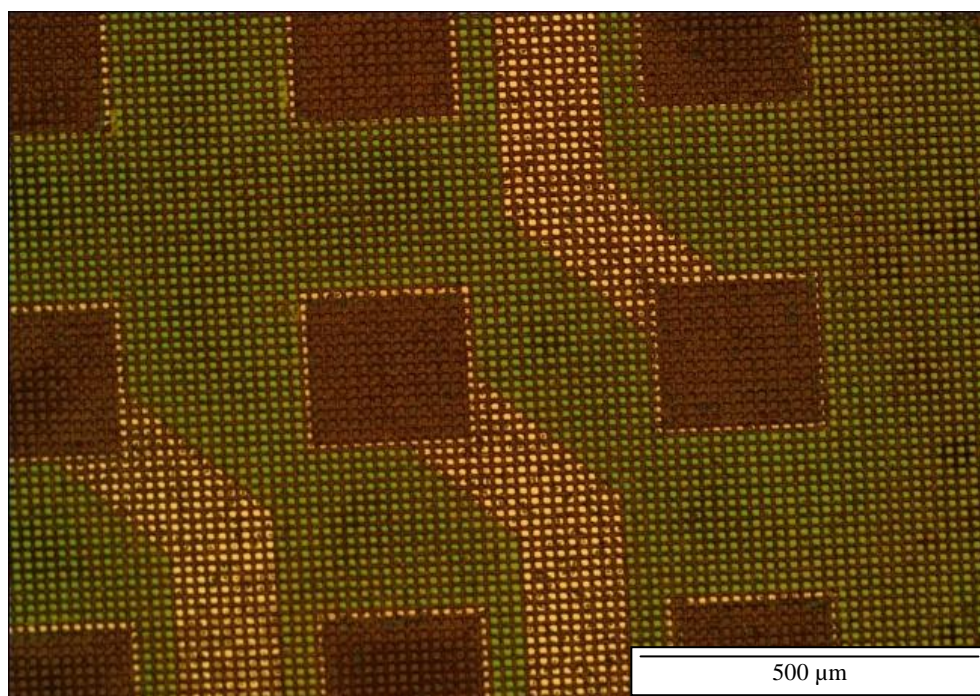
Figure 4.6. The finished cathode and extraction grid after BOE on SiO2.

During the BOE process the Cu grid layer started to delaminate. The SiO_2 could not be properly removed from underneath the grid without additional BOE treatments, as seen in Figure 4.7. Further attempts to help remove the SiO_2 fragments resulted in the Cu grid layer delaminating. The delamination occurred between the high stress Ti seed layer and SiO_2 interface becoming etched away, thus allowing the Ti layer to peel away.
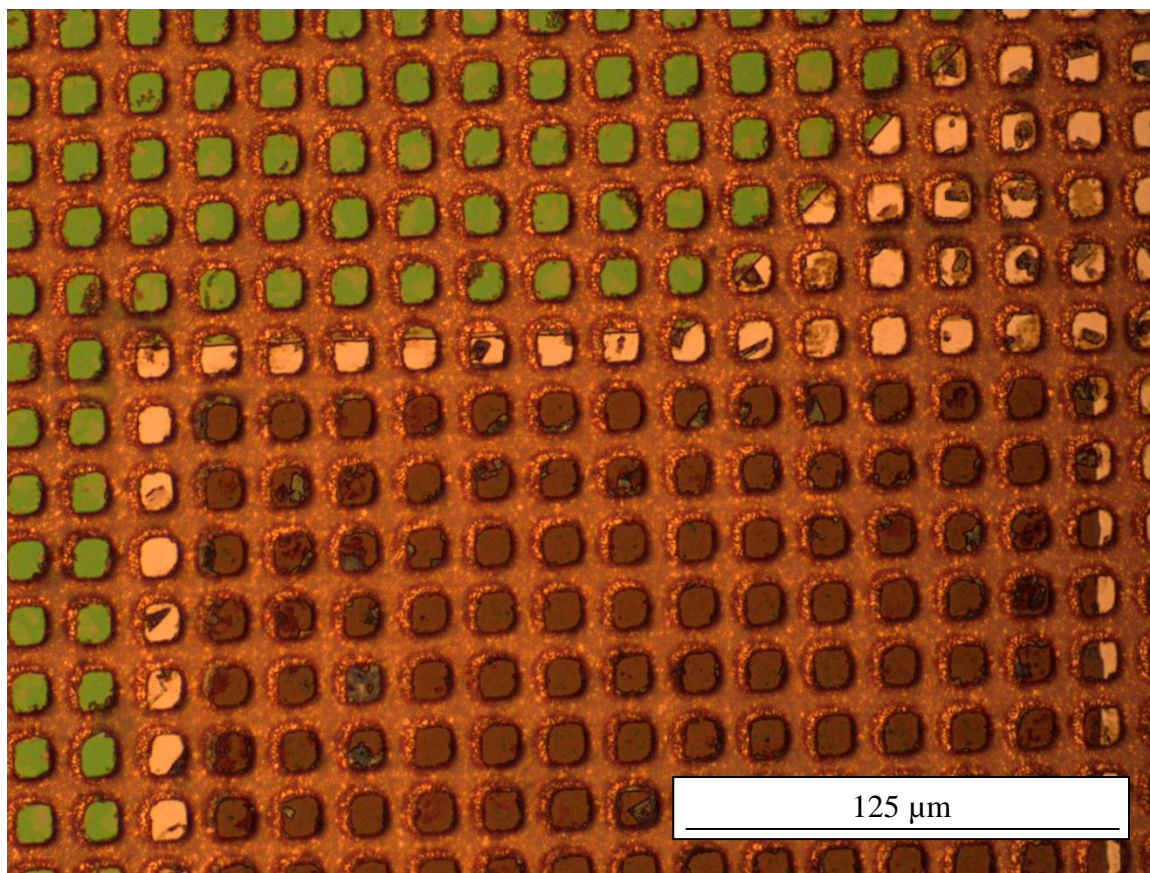
Figure 4.7. Magnified image of a given pixel with SiO_2 fragments remaining.

4.3. ELECTON FIELD EMISSION TESTING

The first step is to electrically connect the grid and N-UNCD pixel. However, due to the copper delamination issue and subsequent harsh undercut to the SiO_2, as seen in Figure 4.6-A, where the copper is missing and the underlying material is exposed; some of the pixels were short circuited. To stop further grid delamination silver epoxy was spread over the grid and several dead pixels for better adhesion. Once the silver epoxy hardened the sample was placed on a Teflon table within a vacuum system, the electrical connections were connected and then the chamber was evacuated, as indicated in Figure 4.8-B. The samples were tested when the pressure was below 4×10^{-8} Torr.
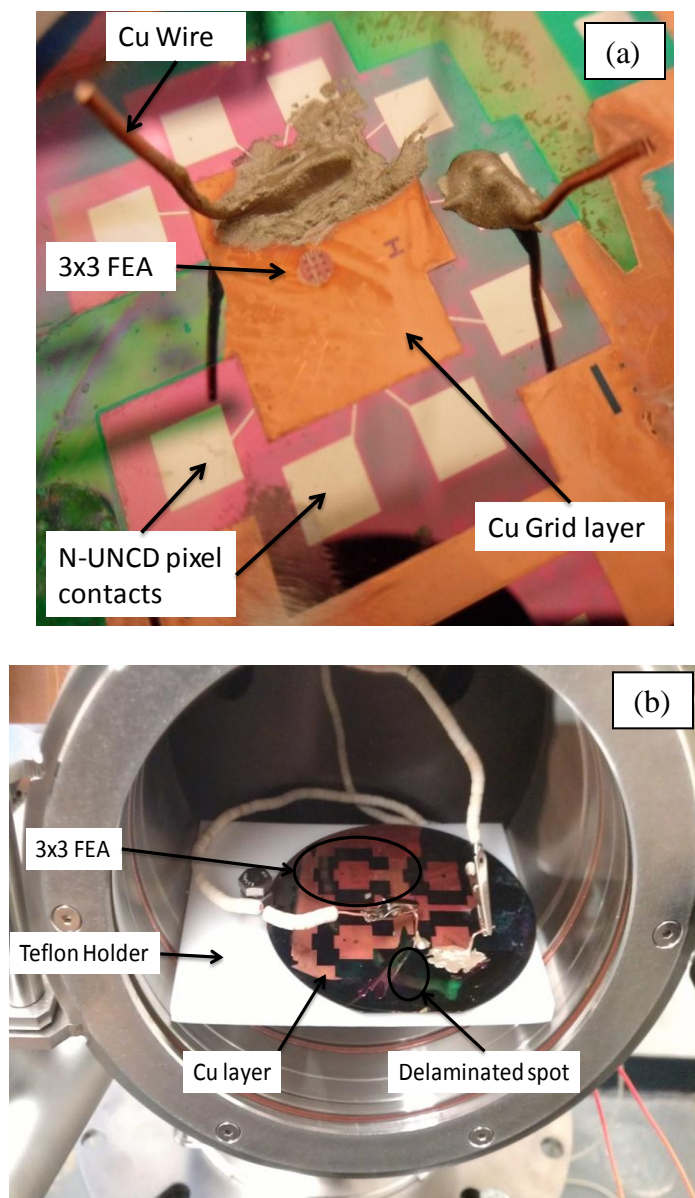
Figure 4.8. Images of the finished cathode and extraction grid with the electrical leads connected. (a) After silver epoxy application. (b) Wafer placed within vacuum chamber with electrical leads connected.

For experimentation the grid was electrically grounded and the voltage fed to the N-UNCD was varied from 0 V to approximately -140 V. A multimeter was used to record the voltage potential between the grid and the cathode. Thus, by knowing the internal resistance of the multimeter the emission current was calculated as seen in Figure 4.9.
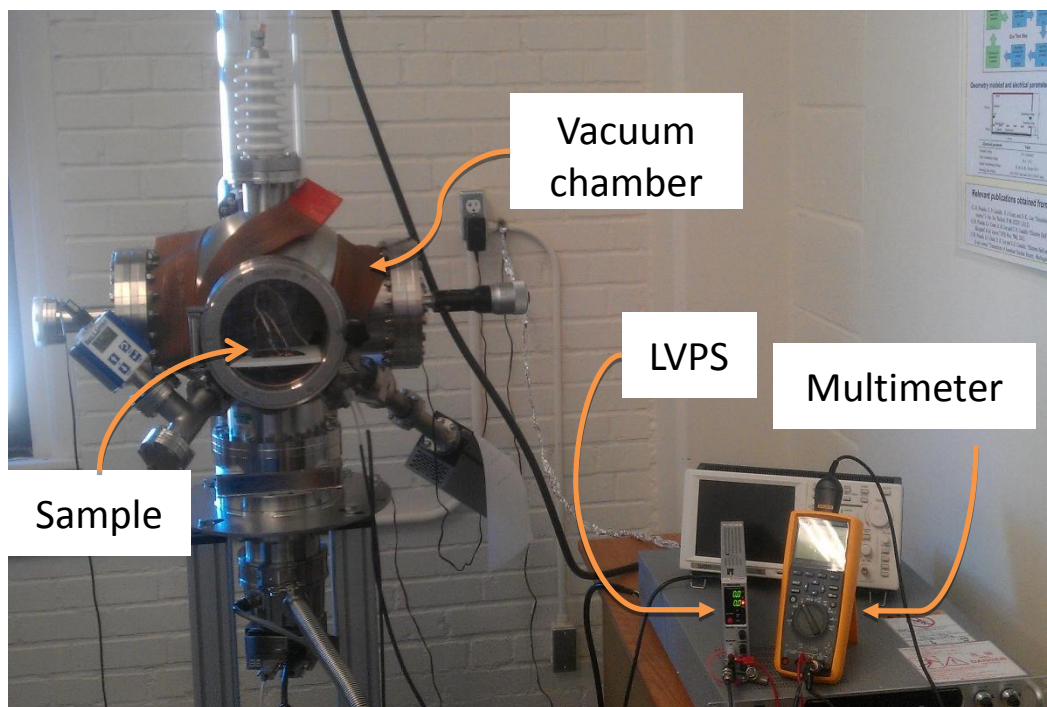
Figure 4.9. Electron field emission testing setup.

In this experiment, two grids were tested and compared: (1) the monolithically fabricated grid by the previously explained procedure, and shown in Figure 4.8-A is Grid I, and (2) a 1000 mesh TEM grid which was silver epoxied directly to the copper electroplated layer. The cathode has a fixed gap of 5 microns between the Grid I and the N-UNCD and a gap of 7 microns between the TEM grid and the N-UNCD. These values were used when estimating the electric field (E). The difference in heights is due to the fact that the TEM grid was silver epoxied on top of the copper layer, which is 2 microns thick.

The field emission can be characterized by Equation 2 as Folwer-Nordheim behavior [28]. The current emission density for the tested samples is seen in Figure 4.10. The current emission density was calculated by the electric current measured at the gate and divided by the active UNCD area for a given pixel. This current density corresponded to a total measured current per pixel of approximately 2 μA at the gate.
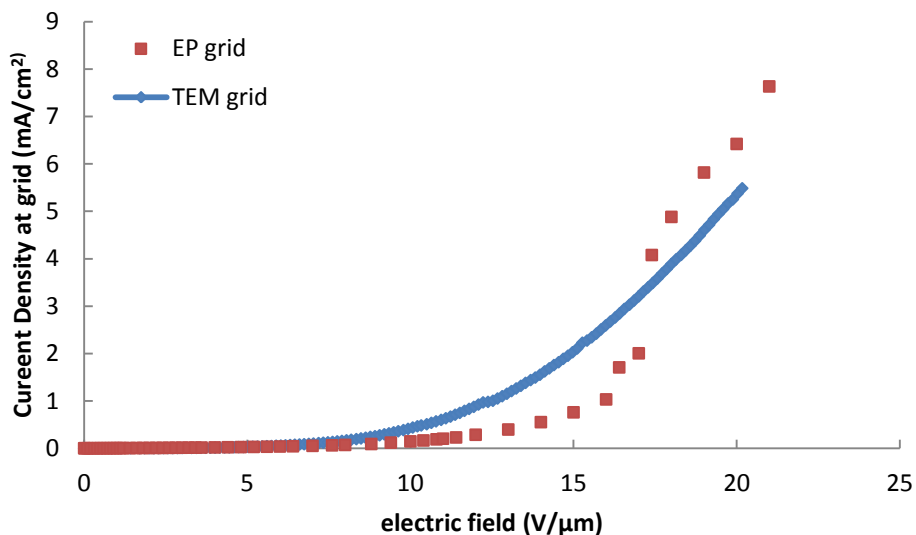
Figure 4.10. The electron current density as measured at the gate, emitted from a given UNCD pixel, as a function of the applied electric field.

The turn on voltage (E_o) for the device was found by fitting linear lines to the high and low fields and then finding their intercept, as seen in Figure 4.11.
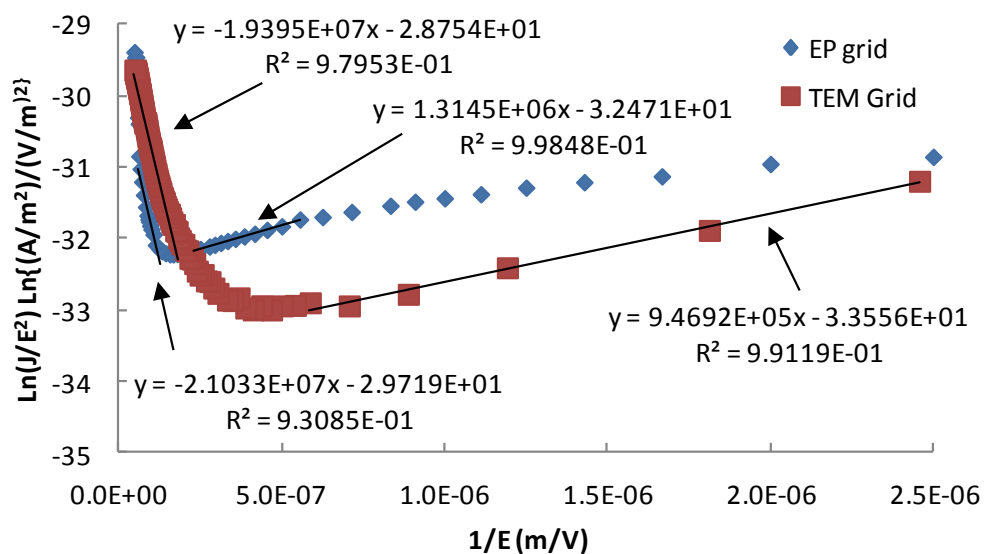
Figure 4.11. F-N Plots of both the EP and TEM grid designs.

Furthermore, the slope of the high field was set equal to the constant term ($B_{FN}.\phi^{3/2}/\beta$) within the exponential in Equation. 1 and the results were plotted in 4.12. The effective work function (ϕ_e) is estimated from the slope of the F-N curve. Such that, the slope divided the constant B_{FN} is equal to the effective work function, as seen in Equation 3.

$$\phi_e = \frac{\phi_{N-UNCD}^{\frac{3}{2}}}{\beta} \tag{3}$$
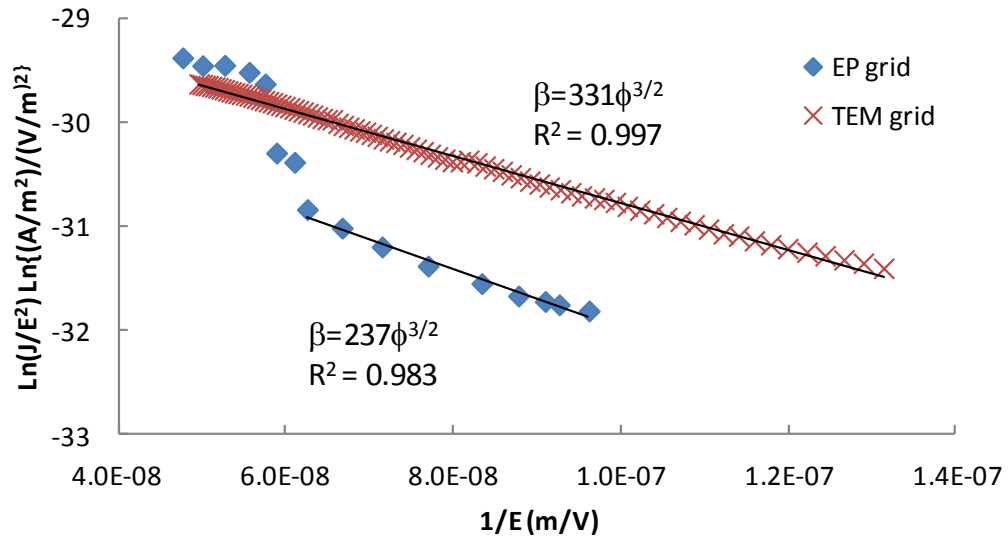
Figure 4.12. Using the FN high field slope to indicate β as a function of ϕ_{UNCD}.

The corresponding values in Table 4.1 match within one order of magnitude with current literature [13-16]. The Grid I sample shows a larger turn-on voltage but quickly matches well with the TEM grid's emission current density after turn-on. This could be from extra SiO_2 between the grid and the UNCD, thus, modifying the electrical field.

Table 4.1. Field emission characteristics of the prototype.

	E_o $(V/\mu m)$[a]	J_e (mA/cm^2)[b]	ϕ_e (eV)[c]
TEM grid	4.69	5.38	0.004
EP grid	8.12	6.42	0.003

[a] Estimated by the intersection of the high and low fields
[b] Emission current density at 20 V/μm
[c] Effective work function estimated from the F-N plot

4.4. ANODE AND CATHODE INTEGRATION

After successfully demonstrating a working cathode, the full triode geometry of a cathode, extraction grid and anode was assembled. However, to continue testing, a commercially available field emission source was purchased, as seen in Figure 4.13.
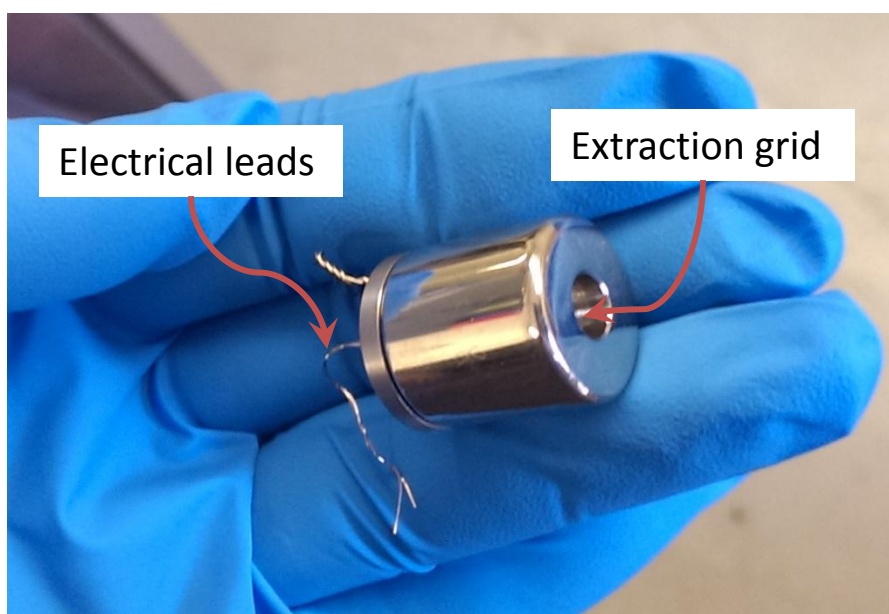
Figure 4.13. Commercially available field emission cold triode cathode by HeatWave Labs, Inc.

A field emission cold triode cathode ATC-CC series (part number 102811) by HeatWave Labs, Inc. allowed fabrication to continue without worrying about destroying the fabricated N-UNCD cathode via voltage breakdown. The source is capable of achieving an electron current of 5 mA operating in continuous DC mode. Additionally, by purchasing the field emission source, it allows us to use a well calibrated electron source for X-ray generation experiments. Using a calibrated source is also important for comparing the simulation work as it is a necessity to know how many electrons are truly bombarding the target. Figure 4.14 shows a sample field emission output current from the field emission source. The field emission source voltage bias was ranged between 0 V and 1200 V. Additionally, by using another electron source with the same approximate electron beam size, the X-ray generation will be identical to our fabricated N-UNCD source.
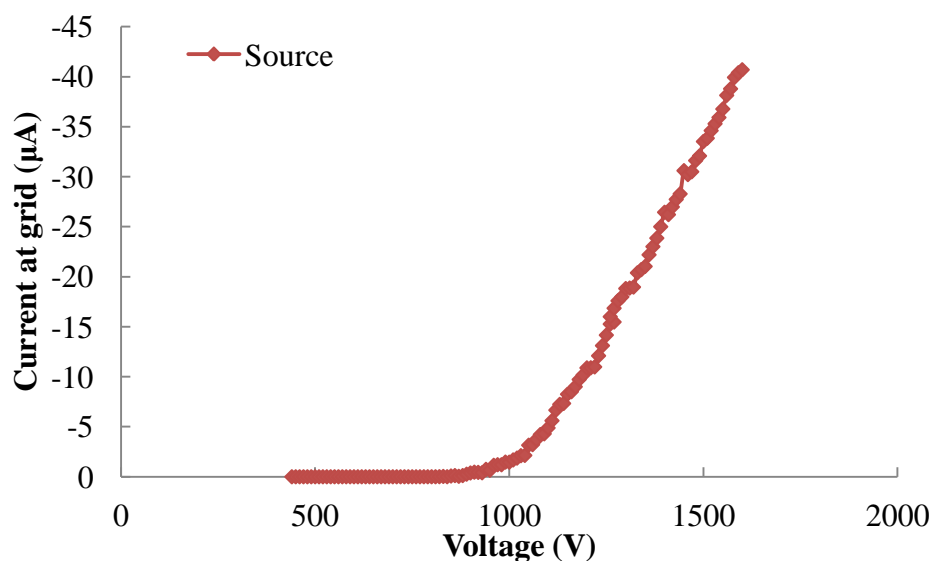
Figure 4.14. Field emission current from the source.

The anode and cathode assembly was built out of Teflon blocks to hold the electron source and anode at a specific distance. Teflon was selected for its high dielectric strength of approximately 20 kV/mm and has a low off gassing rate at ultra low

vacuum pressures. The experimental assembly was then placed inside of the vacuum chamber. The electrical contacts for the field emission source and anode were connected and the voltage sources were turned on, as seen in Figure 4.15.

Figure 4.15. Electron beam visualization via YAG coated glass.

4.5. X-RAY TESTING

In order to start X-ray characterization and testing, a method of X-ray detection outside of the vacuum chamber was envisioned. A custom X-ray detection station was built which allows for easy coupling with the vacuum system, as seen in Figure 4.16. The station was designed such that the X-ray detector, Canberra Lynx system, and X-ray angular collimation devices could be housed together. The Canberra Lynx system was selected as our digital signal processing module since it has several useful capabilities: it acts as a web server for remote use, a built in single channel analyzer (SCA) and multichannel analyzer (MCA) up to 32K channels. All of the Lynx functions can be changed remotely on the fly. So, for example, if we need to change from SCA to MCA mode, we can do so without modifying the experiment. Also, the station allows for the

detector to be moved up and down for alignment with the electron beam. Furthermore, the detector can be positioned such that it can be swept over a large angle to determine the angular distribution of the X-ray output.
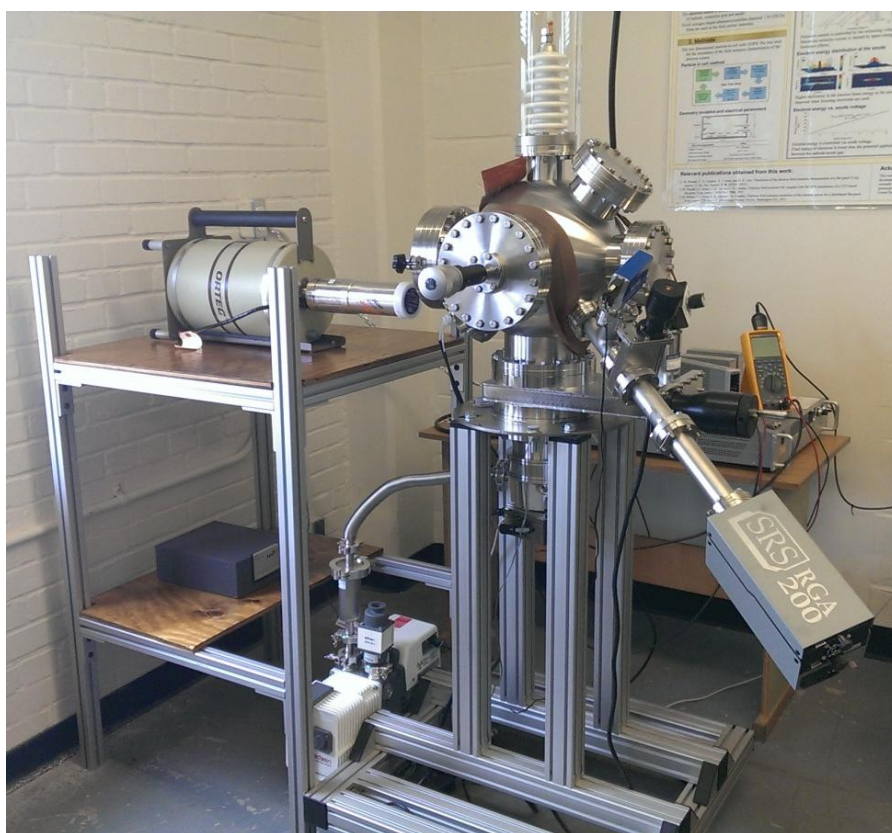
Figure 4.16. X-ray detection table with UHV system.

The X-ray detector selected to determine the angular distribution and energy spectra is the ORTEC GLP-16195-10P4. This detector is capable of energy resolution (full width at half maximum) of 204 eV at 5.9 keV, with an amplifier time constant of 6 μs and operates at a recommended voltage bias of negative 2000 V. What makes the GLP series detectors useful for X-ray detection is their custom end caps which are extremely thin, and our detector was fitted with a 0.127 mm end cap of beryllium which has a very low attenuation coefficient for low energy X-rays, as seen in Figure 4.17.

However, as the end cap is under a vacuum, extreme caution is enforced when handling to make sure the end cap is not ruptured. When the detector is not in use, the end cap protection shield must be installed. Below, Figure 4.17, shows the X-ray detector end cap with a custom lead collimation shield installed during experimentation. To further protect the detector, a plastic spacer was slid over the end guaranteeing the lead shield cannot come in contact with the beryllium window.
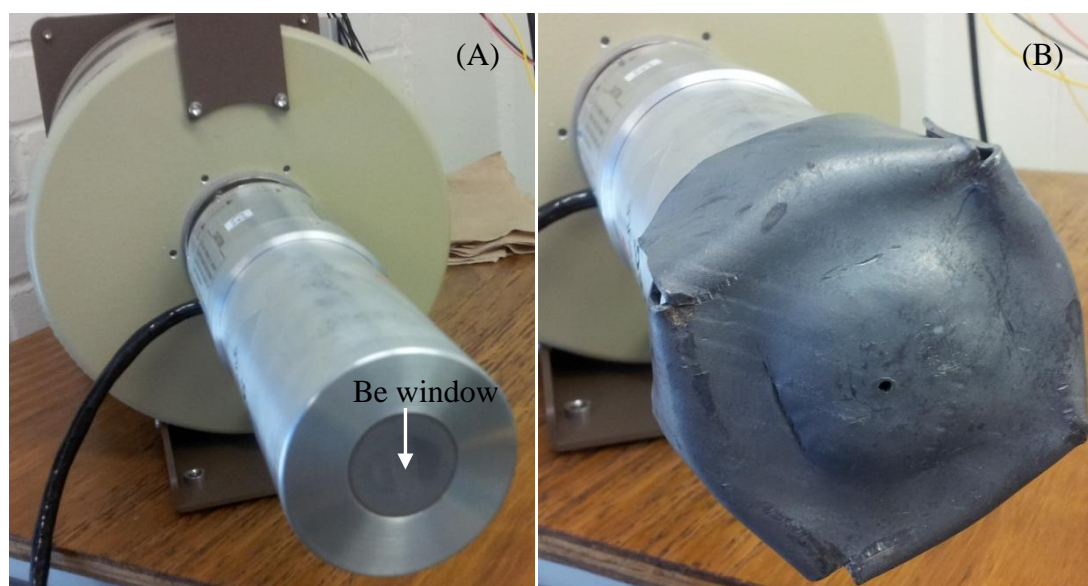
Figure 4.17. Ortec X-ray detector with experimental lead shield in place. (A) without Be window protector and (B) with lead shield and X-ray collimator.

The X-ray detection system has had a full X-ray energy calibration with a Cd-109 source, which itself emits 3 X-rays (88 keV, 25 keV and 22 keV). The energy spectrum shown in Figure 4.18 indicates there are some impurities in the Cd-109 source as the 12 keV peak disappears if the source is removed and counts are collected.
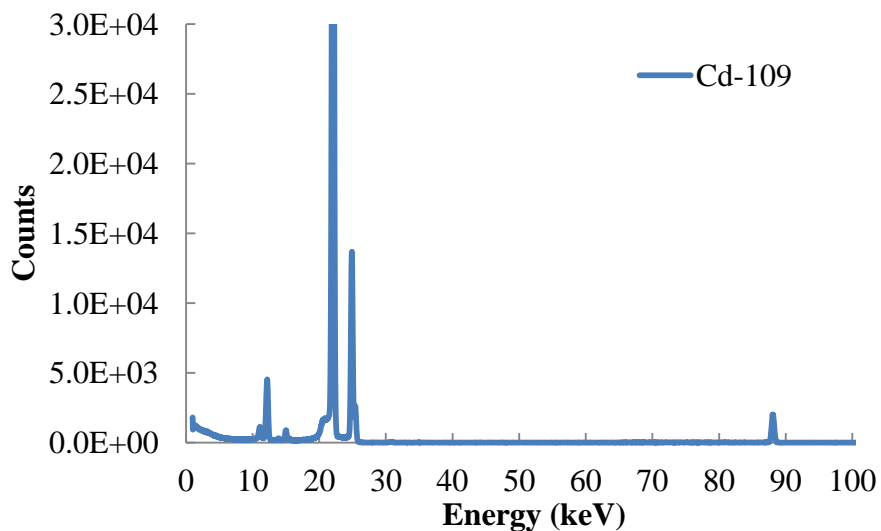
Figure 4.18. Calibrated X-ray energy spectrum from X-ray detection system.

By changing the YAG screen to a 0.5 mm Al-6061 anode with a 700 nm sputtered W target, we were able to produce X-ray results, as shown in Figure 4.19. From the X-ray results, most of the continuous spectrum X-rays below 15 keV are filtered from the anode and vacuum system, as expected. However, the L characteristic X-rays (8-11 keV) are visible. During the experiment, the high voltage power supply was set to 17.1 kVp and X-rays were collected for approximately 1 minute. Then the power supply was increased to 23 kVp to see a change in the Bremsstrahlung maximum energy. The total X-ray counts can be seen on Figure 4.19 (A) and the integrated intensity in Figure 4.19 (B).
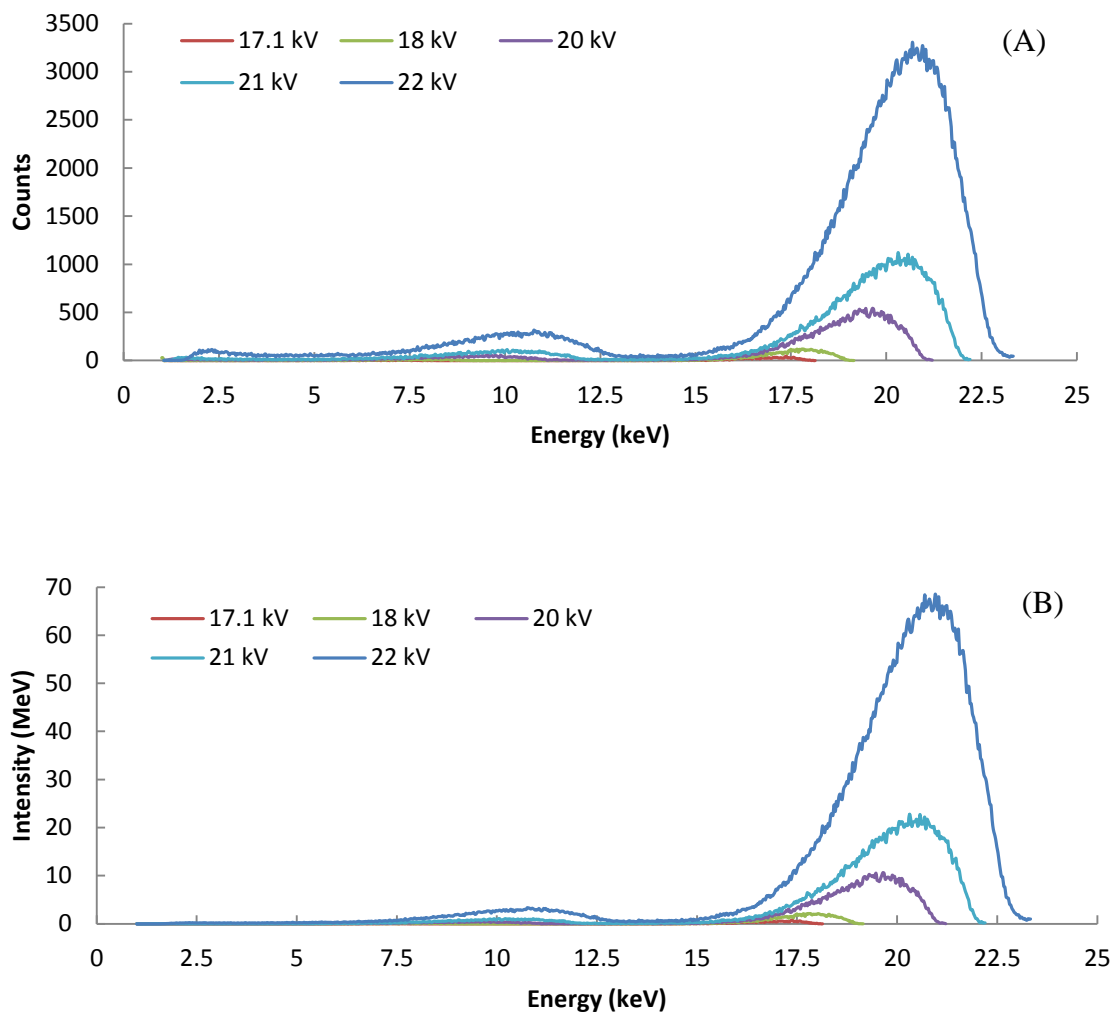
Figure 4.19. X-ray energy (A) and intensity spectrum (B) while the HeatWave electron source operates at 0.85 kV for 30 seconds. Data was collected using the Ortec GLP X-ray detector.

Due to electrical breakdown at the anode, the anode assembly was modified to decrease the frequency of breakdown, while increasing the maximum applied high voltage before breakdown occurs. To decrease the chance for breakdown, several changes were made to the shape of the anode and grooves were added in the Teflon holders. Additionally, the cathode-to-anode distance was increased. Figure 4.20 shows electrical breakdown occurring between the vacuum chamber wall and the anode. Furthermore, you can also see the anode wire quickly heating with possible small plasma

discharge from inside of the ceramic insulators (red glow). In short, by modifying the anode and lowering the electron beam current, the prototype can reach 30 kVp before breakdown.
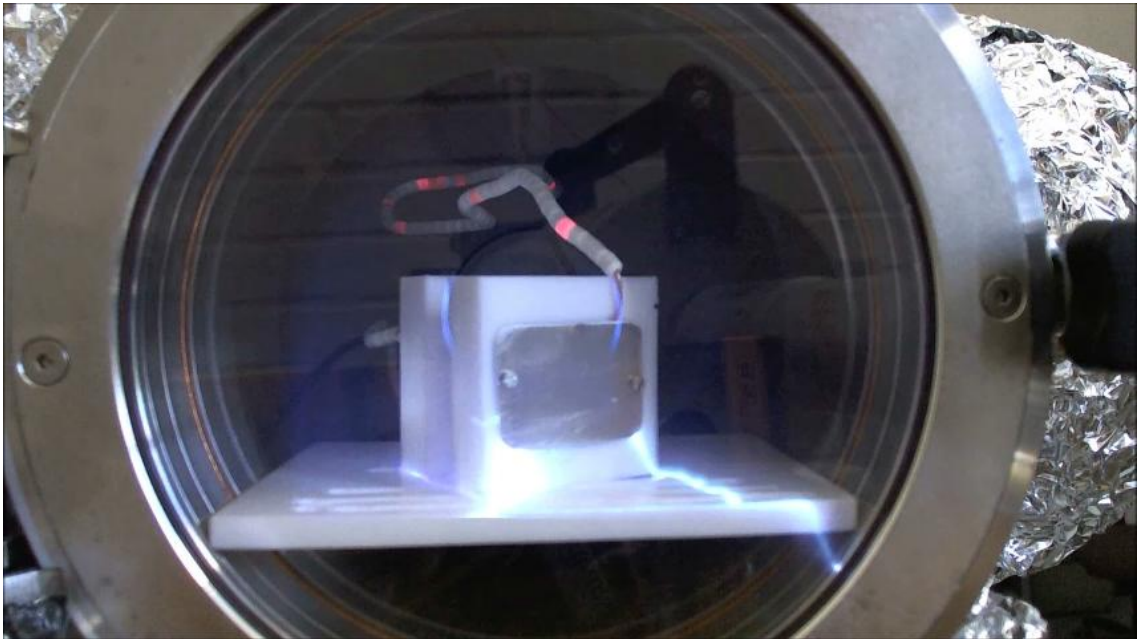
Figure 4.20. Electrical breakdown at 28 kVp with an anode to cathode distance of 15 mm.

By making the indicated changes to the anode assembly, we have successfully increased the X-ray energy up to 30 kVp without electrical breakdown. During the experiment, the high voltage power supply used for electron acceleration was set to 26.9 kVp, and X-rays were collected for approximately 30 seconds. Then, the high voltage was incrementally increased up to 30.2 kV, and energy spectra were recorded along the way. The electron extraction grid bias was held constant at 600 V during the full testing. The recorded X-ray energy spectra are shown in Figure 4.21.
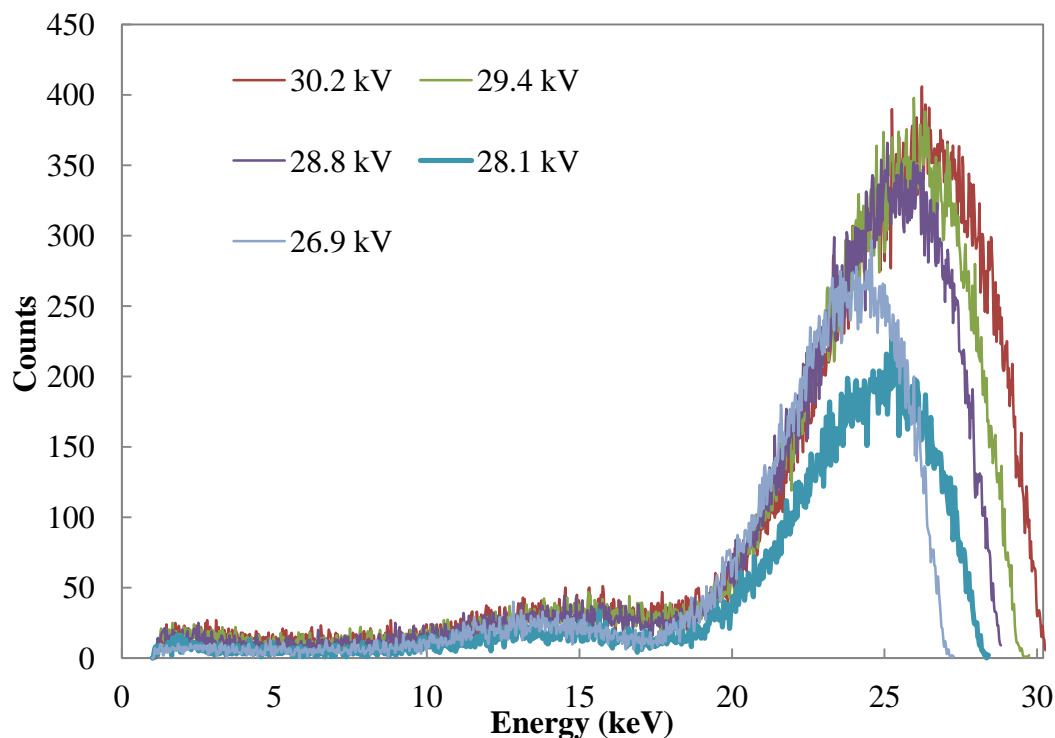
Figure 4.21. X-ray energy spectra from electron beam with energies ranging from 26 keV to 30 keV with a source current of 4.6 nA. Data were collected with Ortec GLP X-ray detector.

To validate/benchmark experimental results, I simulated our full laboratory setup with MCNPX. A MCNPX simulation was modeled and ran with a simplified Kurt Lesker vacuum system geometry. A surface current tally was added at the detector location and X-ray particles were counted as they entered the detector's front surface. Within my MCNPX model, a 30 kVp electron beam struck a 700 nm W target attached to a 2 mm Al-6061 anode; as this simulated the laboratory settings durring the testing in Figure 4.21. One issue that became clear is inablity to resolve the L-shell characterisitic X-ray due to poor low energy sampling with large X-ray attuenation throught the vacuum system. However, the overall shape of the continous Bremsstrahlung X-ray spectrum matches within the MCNPX error bars, as seen in Figure 4.22.
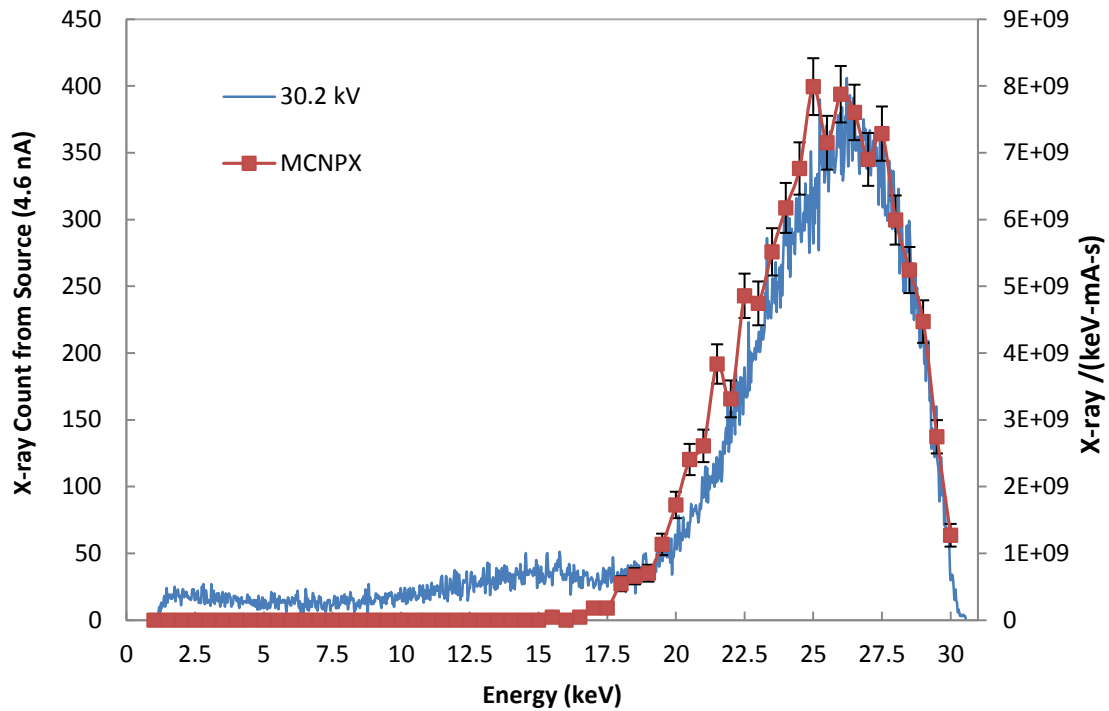
Figure 4.22. A comparison between experimental and MCNPX X-ray energy spectra at the X-ray detector. With an approximate 30 kVp electron beam on a 700 nm W target, in our vacuum system.

Additional work included looking at the behaviour of the X-ray emission in terms of intensity as a function of kVp. In theory, the electrical power from the electical current is

$$P\,(W) = I(mA) \cdot V(kVp). \tag{4}$$

However, not all electrical power is converted into X-rays; another term is used which details this efficiency.

$$conversion = C \cdot z \cdot V(kVp), \tag{5}$$

where C is a proportionally constant and z is the atomic number of the target material being used.

By combining both equation 4 & equation 5, the true X-ray intensity as a function of kVp is found. This indicates there is a quadratic relation between the intensity of X-rays versus the applied high voltage bias.

$$P\ (MeV) \approx C \cdot z \cdot I(mA) \cdot V^2(kVp) \tag{6}$$

By holding the electron beam current constant and keeping the anode material the same, we were able to see that the prototype does operate as expected with equation 6. In Figure 4.23, the measured intensity was curve fitted to a quadratic function. The function fits the data with a R^2=0.9466, thus indicating a properly working anode assembly.
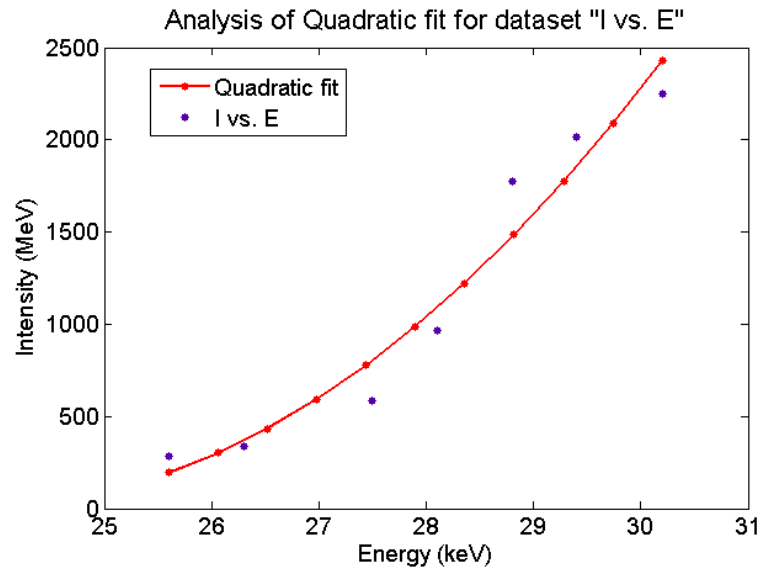
Figure 4.23. Quadratic curve fit of the measured X-ray intensity (MeV) as a function of electron beam energy (kVp).

5. CONCLUSIONS

5.1. MONTE CARLO SIMULATION CONLUSIONS

Through simulations it was demonstrated that micro-sized X-ray tube cells could produce transmission type X-rays by striking a thin (0.25 µm-12 µm) metallic target with high energy electrons. Tungsten was selected as the optimal X-ray target material for both 30 kVp and 100 kVp sources due to its larger output of 1.43×10^{11} MeV/mA-s and 1.48×10^{12} MeV/mA-s, respectively (12.9 % and 10.4 % higher compared to Mo and Rh, respectively). For the transmission X-rays produced, it was shown that either aluminum or copper work well as both an anode and X-ray filter. The X-ray energy spectrum of the flat-panel X-ray source was similar to that of the conventional X-ray tube with the same filtration condition. Electrons with incident direction normal to the target surface produced the highest X-ray output compared to other electron directions. With the same amount of electrons striking the target, higher intensity of X-rays were generated in the forward direction compared to the backward direction, which is a desirable property for the proposed transmission type X-ray source. The backward re-emission of electrons from the target may cause problems with field emission of primary electrons by disturbing the electric field. Further research is needed to help reflect the re-emitted electrons back toward the target to guarantee a proper extraction electric field in the cell and thus maintain a sufficient X-ray yield. A tungsten collimator demonstrated high efficiency. With the aspect ratio ranging from 75 to 125, the intensity of X-rays emitted through neighboring collimator openings was less than 1%, providing suitable pencil X-ray beams. The maximum X-ray intensity after passing through the collimator was around 1×10^7 MeV/mA-s and 1×10^6 MeV/mA-s per pixel for the 100 kVp and 30 kVp

cases, respectively. The proposed flat-panel X-ray source could enable imaging with significantly lower power compared to a conventional X-ray tube. For example, suppose a situation of imaging a large area and thin object using a comparable conventional X-ray tube (100 kVp and 100 mA, i.e., 10 kW) with an image detector with 100 μm pixel pitch located 1 m away would have an X-ray intensity arriving at a pixel of 4.3 x 10^5 MeV/sec. To provide the same intensity of X-ray the flat-panel X-ray source would require only 43 W. Thus, less than 0.5% of the power to operate the conventional X-ray tube is sufficient for the flat-panel X-ray source, for this case. As the power consumption is considerably low, heat generation would not be a significant problem as opposed to conventional X-ray tubes, and passive cooling might be sufficient for the heat removal from the anode plate.

The aspect ratio and the septal thickness of the collimator affect both the collimation efficiency and X-ray intensity. A collimator with a high aspect ratio and thick septa would be suitable for high resolution imaging, while a collimator with a low aspect ratio and thin septa would be utilized for low dose imaging.

5.2. EXPERIMENTAL DESIGN AND TESTING CONCLUSIONS

With this research, the first prototype of a cold cathode array for the flat-panel X-ray source was successfully tested. The results fit well with the simulation studies. Electron beam currents over 1 μA were measured at the electron extraction gate at electric fields lower than 20 V/μm. Additionally X-rays were generated from a tungsten sputtered aluminum 6061 target. There were slight differences between the simulation and recorded X-ray energy spectrum, but the difference may be attributed to the location of the detector outside of the vacuum chamber, thus, further X-ray attenuation occurred

after the glass viewport. A range between 17.1 keV to 30.2 keV was tested at the viewport window and matched well (within a factor of 2). The simulations did not include detector attenuation and energy efficiency but would allow closer agreement to the experiments. Also, the overall shape of the X-ray Bremsstrahlung energy spectrum simulation yielded identical slopes.

5.3. FUTURE WORK

With this work, a first generation prototype was created but there is much work to be completed for a fully working device. A list of topics to pursue and further help the flat-panel X-ray source is explained below.

A. More in-depth heat transfer modeling:

While the heat transfer modeling within this work is a good approximation of maximum heating the target will experience, it is not complete. A good three dimensional transient analysis with a finite element analysis code, such as ABAQUS, is needed for proper thermal characterization. This will better define our current set limits on electron beam size and electron current before anode damage and failure occurs.

B. Experimental X-ray filter optimization:

The currently used filter on the prototype is a 0.02" (0.5 mm) aluminum filter, which was selected for its ability to filter low energy X-ray and to remove heat from the target. However, no optimization study was completed for the prototype, and could be beneficial for X-ray intensities at low kVp where contrast is most important. Furthermore, a study of X-ray filtration quality versus amount

of heat removed could be helpful for higher current operation where thermal damage can occur.

C. Imaging with 2D X-ray detector:

This study was conducted to build and characterize the first prototype flat-panel X-ray source. The electron and X-ray production was characterized, but not its ability for producing radiographs or other imaging modalities. To produce a proper image a large FEA will be needed to demonstrate the design. Nonetheless, simple radiographs could be completed with the HeatWave field emission triode source, but a small flat-panel X-ray detector would be needed over the current GLP POPTOP style Ortec X-ray detector.

D. Multiple focusing gate cathode design:

Our first design only focused on a simple triode style field emission source, but the device could be designed to include focusing lens (gates) which helps focusing the electron beam. In fact, most of the simulation work has been completed by group member Chrystian Posada. Further work would be needed at ANL to fabricate a new FEA cathode with the new focusing lens. Chrystian's work shows that with the new design the electron beam can be made convergent.

E. Incorporating an X-ray anti-scatter grid/collimator:

A micro collimation array needs to be integrated onto the anode assembly. We are currently working with ANL to design and fabricate the anti-scatter grid. Together with Creatv MicroTech, ANL has previously created high-aspect-ratio metallic X-ray collimators with similar dimensions to those needed for our design. We could then integrate their design into our prototype.

APPENDIX A
SAMPLE MCNPX TARGET OPTIMIZATION CODE

```
continue
C ----------------------------------------------------------------------------
C                    Edwin Grant
C                      6/27/10
C Info:
C This model looks at one cell of an mock flat panel X-ray generator
C   with Electron physics
C
C ----------------------------------------------------------------------------
C                    Cell Cards
C ----------------------------------------------------------------------------
C
C  W Target 1st of 5 segments
1  1 -19.3   1 -2 -15 16 -17 18    imp:p=1 imp:e=1  $ tungsten target
C W Target 2nd of 5 segments
2  1 -19.3   2 -3 -15 16 -17 18    imp:p=1 imp:e=1  $ tungsten target
C W Target 3rd of 5 segments
3  1 -19.3   3 -4 -15 16 -17 18    imp:p=1 imp:e=1  $ tungsten target
C W Target 4th of 5 segments
4  1 -19.3   4 -5 -15 16 -17 18    imp:p=1 imp:e=1  $ tungsten target
C W Target 5th of 5 segments
5  1 -19.3   5 -6 -15 16 -17 18    imp:p=1 imp:e=1  $ tungsten target
C bottom void for electron counting/beam
6 0      -15 16 -17 18 -1 100    imp:p=0 imp:e=1  $ Vacuum
C top void for photon counting
7 0      -15 16 -17 18 6 -101    imp:p=1 imp:e=0  $ Vacuum
C
C particle killer
8 0 -100:101:15:-16:17:-18        imp:p=0 imp:e=0  $ Vacuum
C


C
C Surface Cards
C -------------
C Z sides
1  pz 0.00000    $ bottom of Tungsten target
2  pz 0.00009 $ top of tungsten target (.4 microns thick)
3  pz 0.00018 $ top of tungsten target (.8 microns thick)
4  pz 0.00027 $ top of tungsten target (1.2 microns thick)
5  pz 0.00036 $ top of tungsten target (1.6 microns thick)
6  pz 0.00045 $ top of tungsten target (2 microns thick)
C
C x sides
15 px  0.005     $ positive x side of tungsten
16 px -0.005     $ Negative x side of tungsten
C Y sides
17 py 0.005      $ positive y side of tungsten
18 py -0.005     $ Negative y side of tungsten
C
C
C fake z sides for tallies
100  pz -0.0002   $ for source electrons counting
101  pz  0.0005   $ for leaving gamma rays
```

```
C

C ------------------------------------------------------------------------
C                    Data Cards
C ------------------------------------------------------------------------
C
C        ************* SOURCE INFORMATION ******************
mode e p
C point source of 100 keV Electrons in the + Z direction @ (0,0,-0.0001)
sdef erg=0.1 POS=0 0 -0.0001 VEC=0 0 1 AXS=0 0 1 RAD=D1 DIR=1 PAR=3
C  OOPIC-PRO ELECTRON DIST.
SI1   0.0000001
     0.00006
     0.00012
     0.00018
     0.00024
     0.0003
     0.00036
     0.00042
     0.00048
     0.00054
     0.0006
     0.00066
     0.00072
     0.00078
     0.00084
     0.0009
     0.00096
     0.00102
     0.00108
     0.00114
     0.0012
     0.00126
     0.00132
     0.00138
     0.00144
     0.0015
     0.00156
     0.00162
     0.00168
     0.00174
     0.0018
     0.00186
     0.00192
     0.00198
     0.00204
     0.0021
     0.00216
     0.00222
     0.00228
     0.00234
     0.0024
     0.00246
```

0.00252
0.00258
0.00264
0.0027
0.00276
0.00282
0.00288
0.00294
0.003
0.00306
0.00312
0.00318
0.00324
0.0033
0.00336
0.00342
0.00348
0.00354
0.0036
0.00366
0.00372
0.00378
0.00384
0.0039
0.00396
0.00402
0.00408
0.00414
0.0042
0.00426
0.00432
0.00438
0.00444
0.0045
0.00456
0.00462
SP1   0
0.926991106
0.919733944
0.923400636
0.953821343
0.955815157
0.955450092
0.945091888
0.949496732
0.937457626
0.922915221
0.921097922
0.928812417
0.916283884
0.903358192
0.903663082
0.925542883

0.927913797
0.918710961
0.918682879
0.989228591
0.998495613
0.887006511
0.813604471
0.927713212
0.90984912
0.928050194
0.874032679
0.458015573
0.413409502
0.416863574
0.419402979
0.148523495
0
0
0
0
0
0
0
0
0
0
0
0
0
0
0
0
0
0
0
0
0
0
0
0
0
0
0
0
0
0
0
0
0

```
        0
        0
        0
        0
        0
        0
        0
        0
C
PHYS:E 0.10 0 0 0 0 0 1 1 0 1 0
C
C
C wwg 21 6
C
C
NPS 100E6
C
C ***********************************************************************
C Tallies
C -------
C
C
C Photon counting from top of W target
C -----------------------------------------------------------------------------
C UNITS of Particles
*F11:P 6
FM11  6.242E15  $ e- per mC
FC11   Total Photon Output
C -----------------------------------------------------------------------------
C Photon counting from top of W target
C -----------------------------------------------------------------------------
C UNITS of Particles
*F21:P 6
*C21  90 80 70 60 50 40 30 20 10 0
FM21  6.242E15  $ e- per mC
FC21   This Tally breaks the Photon INTENSITY from surface 2 into angles
       electrons direction from source and backscatter "level surface 1"
C -----------------------------------------------------------------------------
C UNITS of MeV
F31:P 6
E31    1E-3  2E-3  3E-3  4E-3  5E-3  6E-3  7E-3  8E-3  9E-3 10E-3
      11E-3 12E-3 13E-3 14E-3 15E-3 16E-3 17E-3 18E-3 19E-3 20E-3
      21E-3 22E-3 23E-3 24E-3 25E-3 26E-3 27E-3 28E-3 29E-3 30E-3
      31E-3 32E-3 33E-3 34E-3 35E-3 36E-3 37E-3 38E-3 39E-3 40E-3
      41E-3 42E-3 43E-3 44E-3 45E-3 46E-3 47E-3 48E-3 49E-3 50E-3
      51E-3 52E-3 53E-3 54E-3 55E-3 56E-3 57E-3 58E-3 59E-3 60E-3
      61E-3 62E-3 63E-3 64E-3 65E-3 66E-3 67E-3 68E-3 69E-3 70E-3
      71E-3 72E-3 73E-3 74E-3 75E-3 76E-3 77E-3 78E-3 79E-3 80E-3
      81E-3 82E-3 83E-3 84E-3 85E-3 86E-3 87E-3 88E-3 89E-3 90E-3
      91E-3 92E-3 93E-3 94E-3 95E-3 96E-3 97E-3 98E-3 99E-3 100E-3
FM31  6.242E15  $ e- per mC
FC31  This Tally is the bremsstrahlung energy spectrum
C
```

```
C ************************************************************************
C Material
C --------
C Target
 M1   74000.04p 1  $ Tungsten    rho=19.3 g/cc
C M2 42000.04p 1  $ Molybdenum  rho=10.22 g/cc
C M3 45000.04p 1  $ Rhodium     rho=12.41 g/cc
C
C End of File
```

APPENDIX B

SAMPLE MCNPX LARGE ARRAY COLLIMATION CODE

continue
C ---
C   Edwin Grant
C   5/27/11
C Info:
C This model looks at an array of a mock flat panel X-ray generator
C
C   Aspect ratio 75 & septal thickness of 60 microns
C ---
C   Cell Cards
C ---
C
C W Target 1st of 5 segments
1 1 -19.3   1 -2 -2000   U=2 imp:p=0 imp:e=0 $ tungsten target
C W Target 2nd of 5 segments
2 1 -19.3   2 -3 -2000 U=2 imp:p=0 imp:e=0 $ tungsten target
C W Target 3rd of 5 segments
3 1 -19.3   3 -4 -2000   U=2 imp:p=0 imp:e=0 $ tungsten target
C W Target 4th of 5 segments
4 1 -19.3   4 -5 -2000   U=2 imp:p=0 imp:e=0 $ tungsten target
C W Target 5th of 5 segments
5 1 -19.3   5 -6 -2000   U=2 imp:p=0 imp:e=0 $ tungsten target
C Cu Filter 5th of 5 segments
50 7 -8.94   6 -7 -2000   U=2 imp:p=0 imp:e=0 $ tungsten target
C bottom void for electron counting/beam
6 0   -1 100 -2000 U=2   imp:p=0 imp:e=0 $ Vacuum
C collimation square
7 1 -19.3 (25:-26:27:-28) 7   U=2 imp:p=1 imp:e=0
C air inside collimation
8 5 -0.0012 (-25 26 -27 28) 7   U=2 imp:p=1 imp:e=0 $ Air
C below pixel
11 5 -0.0012 -2000 -100 imp:p=0 imp:e=0 U=2 $ Air
C
C
C Void around flat panel
200 5 -0.0012 -200 imp:p=1 imp:e=0 u=3
C
C Pixel Array
 1000 0 -15 16 -17 18 lat=1 U=10 fill=-401:401 -401:401 0:0
     2 644808r   imp:p=1 imp:e=1
C Box for array
 300 0 -300 301 -302 303 -304 305 imp:p=1 imp:e=0 fill=10
 301 5 -0.0012 -9999 #300   imp:p=1 imp:e=0 $ ##CHANGE IMPORT##
C particle killer
 9999 0 9999   imp:p=0 imp:e=0 $ Vacuum
C

C *************
C Surface Cards
C *************
C
2000 cz 5
C For standard pixel U=2

```
C ------------------
C Target z thicknesses
1  pz 0.00000   $ bottom of Tungsten target
2  pz 0.00009 $ top of tungsten target (.4 microns thick)
3  pz 0.00018 $ top of tungsten target (.8 microns thick)
4  pz 0.00027 $ top of tungsten target (1.2 microns thick)
5  pz 0.00036 $ top of tungsten target (1.6 microns thick)
6  pz 0.00045 $ top of tungsten target (2 microns thick)
C
C  TOP OF FILTER
7  pz 0.05045  $ top of The filter
C
C *** Pixel size  Surfs 15-18 ***
C x sides
15 px  0.005     $ positive x side of tungsten
16 px -0.005     $ Negative x side of tungsten
C Y sides
17 py 0.005      $ positive y side of tungsten
18 py -0.005     $ Negative y side of tungsten
C
C *** Collimation walls  Surfs 25-28 ***
C x sides
25 px  0.002     $ positive x side of tungsten
26 px -0.002     $ Negative x side of tungsten
C Y sides
27 py  0.002      $ positive y side of tungsten
28 py -0.002     $ Negative y side of tungsten
C
C
C Top of collimator
C -----------------
24 pz 0.35045       $ (4.5 mic + 0.5 mm + 0.625 cm tall collimation wall
C
C For bottom void
100  pz -0.0002   $ for source electrons counting
C ===============================================
C
C For air around flat panel U=3
C ----------------------------
200 cz 1
C ===============================================
C
C
C *** !!!!!!!!!!!!!!!!!!!!!!!!!!!!!!!!!!!!!! ****
C Box to fill Array  (in next 6 surfaces)
C *** !!!!!!!!!!!!!!!!!!!!!!!!!!!!!!!!!!!!!! ****
C
300 px  4.005
301 px -4.005
302 py  4.005
303 py -4.005
304 pz  0.35045
305 pz -0.3
```

```
C ================================================
C
C Outer partical killer
C ---------------------
9999 1 so 25
C ================================================
C
C
C fake z sides for tallies
C Allows for 2 degree bins on spherical tally
C /\/\/\/\/\/\/\/\/\/\
 501 1 pz 24.98477068
 502 1 pz 24.93910126
 503 1 pz 24.86304738
 504 1 pz 24.75670172
 505 1 pz 24.62019383
 506 1 pz 24.45369002
 507 1 pz 24.25739316
 508 1 pz 24.0315424
 509 1 pz 23.77641291
 510 1 pz 23.49231552
 511 1 pz 23.17959636
 512 1 pz 22.83863644
 513 1 pz 22.46985116
 514 1 pz 22.07368982
 515 1 pz 21.65063509
 516 1 pz 21.2012024
 517 1 pz 20.72593931
 518 1 pz 20.22542486
 519 1 pz 19.70026884
 520 1 pz 19.15111108
 521 1 pz 18.57862064
 522 1 pz 17.98349501
 523 1 pz 17.36645926
 524 1 pz 16.72826516
 525 1 pz 16.06969024
 526 1 pz 15.39153688
 527 1 pz 14.69463131
 528 1 pz 13.97982259
 529 1 pz 13.24798161
 530 1 pz 12.5
 531 1 pz 11.73678907
 532 1 pz 10.95927867
 533 1 pz 10.16841608
 534 1 pz 9.365164835
 535 1 pz 8.550503583
 536 1 pz 7.725424859
 537 1 pz 6.890933895
 538 1 pz 6.04804739
 539 1 pz 5.19779227
 540 1 pz 4.341204442
 541 1 pz 3.479327524
 542 1 pz 2.613211582
```

```
 543 1 pz 1.743911844
 544 1 pz 0.872487418
C
C fake TALLY surfaces for top of collimation
C -----------------------------------
C  for columns (Sets Y heights)  * change value if col. Thickness changes *
C
C  Top Column  (0)     (5 above home)
2700 300 py  0.002
2800 300 py -0.002
C     Column  (1)    (4 above home)
2701 301 py  0.002
2801 301 py -0.002
C     Column  (2)    (3 above home)
2702 302 py  0.002
2802 302 py -0.002
C     Column  (3)    (2 above home)
2703 303 py  0.002
2803 303 py -0.002
C     Column  (4)    (1 above home)
2704 304 py  0.002
2804 304 py -0.002
C
C here is "home" column as defined with just surfs 27,28
C
C     Column  (6)    (1 below home)
2706 306 py  0.002
2806 306 py -0.002
C     Column  (7)    (2 below home)
2707 307 py  0.002
2807 307 py -0.002
C     Column  (8)    (3 below home)
2708 308 py  0.002
2808 308 py -0.002
C     Column  (9)    (4 below home)
2709 309 py  0.002
2809 309 py -0.002
C     Column  (10)   (5 below home)
2710 310 py  0.002
2810 310 py -0.002
C
C
C Right Wall  *** To change collimator thickness just change px value ***
C left of center pixel
2501  201   px 0.002
2502  202   px 0.002
2503  203   px 0.002
2504  204   px 0.002
2505  205   px 0.002
2506  206   px 0.002
2507  207   px 0.002
2508  208   px 0.002
2509  209   px 0.002
```

```
2510  210    px 0.002
C Right of center pixel
2551  101    px 0.002
2552  102    px 0.002
2553  103    px 0.002
2554  104    px 0.002
2555  105    px 0.002
2556  106    px 0.002
2557  107    px 0.002
2558  108    px 0.002
2559  109    px 0.002
2560  110    px 0.002
C
C Left Wall
C Left of center pixel
2601  201    px -0.002
2602  202    px -0.002
2603  203    px -0.002
2604  204    px -0.002
2605  205    px -0.002
2606  206    px -0.002
2607  207    px -0.002
2608  208    px -0.002
2609  209    px -0.002
2610  210    px -0.002
C
C Right of center pixel
2651  101    px -0.002
2652  102    px -0.002
2653  103    px -0.002
2654  104    px -0.002
2655  105    px -0.002
2656  106    px -0.002
2657  107    px -0.002
2658  108    px -0.002
2659  109    px -0.002
2660  110    px -0.002


C ---------------------------------------------------------------------------
C                     Data Cards
C ---------------------------------------------------------------------------
C
C Transform to move sphere up to top of anode surface
TR1    0 0 0.00045
C transforms for pixel wall collimators assuming 100 micron pixel pitch
C
C for Row pixels right of center
TR101  0.01 0 0
TR102  0.02 0 0
TR103  0.03 0 0
TR104  0.04 0 0
TR105  0.05 0 0
TR106  0.06 0 0
```

TR107 0.07 0 0
TR108 0.08 0 0
TR109 0.09 0 0
TR110 0.1 0 0
C for Row pixels left of center
TR201 -0.01 0 0
TR202 -0.02 0 0
TR203 -0.03 0 0
TR204 -0.04 0 0
TR205 -0.05 0 0
TR206 -0.06 0 0
TR207 -0.07 0 0
TR208 -0.08 0 0
TR209 -0.09 0 0
TR210 -0.1 0 0
C
C for column pixels
TR300 0 0.05 0 $ Top column (0)
TR301 0 0.04 0 $ column (1)
TR302 0 0.03 0 $ column (2)
TR303 0 0.02 0 $ column (3)
TR304 0 0.01 0 $ column (4)
C   "CENTER"
TR306 0 -0.01 0 $ column (6)
TR307 0 -0.02 0 $ column (7)
TR308 0 -0.03 0 $ column (8)
TR309 0 -0.04 0 $ column (9)
TR310 0 -0.05 0 $ column (10)
C
C
C
C   ************* SOURCE INFORMATION *****************
mode p
C 2 Pi source of 100 keV photon in the + Z direction
C
SDEF ERG=0.1 pos=0 0 0.050451 VEC=0 0 1 AXS=0 0 1 rad=0.0024
PHYS:p 0.10 0 0 0 0 0 1 1 0 1 0
C
C
DBCN 12j 18500
C
C wwg 551 0
C
C MESH GEOM=rec origin= -0.005 -0.005 -0.00011 imesh=0.005 iints=50
C   jmesh=0.005 jints=50 kmesh= 0 0.00045 0.05045 1.05045 kints=1 5 10 1
C   ref=0 0 0
C
C For Better BBREM Results
 BBREM 1. 1. 46I 10. 1
C
C
C Source read card
C this reads photons crossing over surface 7

```
C  SSW  7(-50) sym=2 PTY=P
C  SSR old=7
C
C
NPS 500E6
prdmp 2j 1
C
C *********************************************************************
C Tallies
C -------
C
C tally for pixel bleed off between cells
C -------------------------------------
C
C COLUMN 0
FC01 pixel C0-R0
F01:P 24
FS01 -2603 2503 2702 -2802
FM01 6.24E+15
C
FC11 pixel C0-R1
F11:P 24
FS11 -2602 2502 2702 -2802
FM11 6.24E+15
C
FC21 pixel C0-R2
F21:P 24
FS21 -2601 2501 2702 -2802
FM21 6.24E+15
C
FC31 C0-CENTER PIXEL
F31:P 24
FS31 -26 25 2702 -2802
FM31 6.24E+15
C
FC41 pixel C0-R4
F41:P 24
FS41 -2651 2551 2702 -2802
FM41 6.24E+15
C
FC51 pixel C0-R5
F51:P 24
FS51 -2652 2552 2702 -2802
FM51 6.24E+15
C
FC61 pixel C0-R6
F61:P 24
FS61 -2653 2553 2702 -2802
FM61 6.24E+15
C
C *********************************************************************
C
C COLUMN 1
```

```
FC101 pixel C1-R0
F101:P 24
FS101 -2603 2503 2703 -2803
FM101 6.24E+15
C
FC111 pixel C1-R1
F111:P 24
FS111 -2602 2502 2703 -2803
FM111 6.24E+15
C
FC121 pixel C1-R2
F121:P 24
FS121 -2601 2501 2703 -2803
FM121 6.24E+15
C
FC131 C1-CENTER PIXEL
F131:P 24
FS131 -26 25 2703 -2803
FM131 6.24E+15
C
FC141 pixel C1-R4
F141:P 24
FS141 -2651 2551 2703 -2803
FM141 6.24E+15
C
FC151 pixel C1-R5
F151:P 24
FS151 -2652 2552 2703 -2803
FM151 6.24E+15
C
FC161 pixel C1-R6
F161:P 24
FS161 -2653 2553 2703 -2803
FM161 6.24E+15
C
C *********************************************************************
C
C COLUMN 2
FC201 pixel C2-R0
F201:P 24
FS201 -2603 2503 2704 -2804
FM201 6.24E+15
C
FC211 pixel C2-R1
F211:P 24
FS211 -2602 2502 2704 -2804
FM211 6.24E+15
C
FC221 pixel C2-R2
F221:P 24
FS221 -2601 2501 2704 -2804
FM221 6.24E+15
C
```

```
FC231 C2-CENTER PIXEL
F231:P 24
FS231 -26 25 2704 -2804
FM231 6.24E+15
C
FC241 pixel C2-R4
F241:P 24
FS241 -2651 2551 2704 -2804
FM241 6.24E+15
C
FC251 pixel C2-R5
F251:P 24
FS251 -2652 2552 2704 -2804
FM251 6.24E+15
C
FC261 pixel C2-R6
F261:P 24
FS261 -2653 2553 2704 -2804
FM261 6.24E+15
C
C *****************************************************************
C
C COLUMN 3
FC301 pixel C3-R0
F301:P 24
FS301 -2603 2503 27 -28
FM301 6.24E+15
C
FC311 pixel C3-R1
F311:P 24
FS311 -2602 2502 27 -28
FM311 6.24E+15
C
FC321 pixel C3-R2
F321:P 24
FS321 -2601 2501 27 -28
FM321 6.24E+15
C
FC331 C3-CENTER PIXEL
F331:P 24
FS331 -26 25 27 -28
FM331 6.24E+15
C
FC341 pixel C3-R4
F341:P 24
FS341 -2651 2551 27 -28
FM341 6.24E+15
C
FC351 pixel C3-R5
F351:P 24
FS351 -2652 2552 27 -28
FM351 6.24E+15
C
```

```
FC361 pixel C3-R6
F361:P 24
FS361 -2653 2553 27 -28
FM361 6.24E+15
C
C ***********************************************************************
C
C COLUMN 4
FC401 pixel C4-R0
F401:P 24
FS401 -2603 2503 2706 -2806
FM401 6.24E+15
C
FC411 pixel C4-R1
F411:P 24
FS411 -2602 2502 2706 -2806
FM411 6.24E+15
C
FC421 pixel C4-R2
F421:P 24
FS421 -2601 2501 2706 -2806
FM421 6.24E+15
C
FC431 C4-CENTER PIXEL
F431:P 24
FS431 -26 25 2706 -2806
FM431 6.24E+15
C
FC441 pixel C4-R4
F441:P 24
FS441 -2651 2551 2706 -2806
FM441 6.24E+15
C
FC451 pixel C4-R5
F451:P 24
FS451 -2652 2552 2706 -2806
FM451 6.24E+15
C
FC461 pixel C4-R6
F461:P 24
FS461 -2653 2553 2706 -2806
FM461 6.24E+15
C
C ***********************************************************************
C
C COLUMN 5
FC501 pixel C5-R0
F501:P 24
FS501 -2603 2503 2707 -2807
FM501 6.24E+15
C
FC511 pixel C5-R1
F511:P 24
```

```
FS511 -2602 2502 2707 -2807
FM511 6.24E+15
C
FC521 pixel C5-R2
F521:P 24
FS521 -2601 2501 2707 -2807
FM521 6.24E+15
C
FC531 C5-CENTER PIXEL
F531:P 24
FS531 -26 25 2707 -2807
FM531 6.24E+15
C
FC541 pixel C5-R4
F541:P 24
FS541 -2651 2551 2707 -2807
FM541 6.24E+15
C
FC551 pixel C5-R5
F551:P 24
FS551 -2652 2552 2707 -2807
FM551 6.24E+15
C
FC561 pixel C5-R6
F561:P 24
FS561 -2653 2553 2707 -2807
FM561 6.24E+15
C
C ********************************************************************
C
C COLUMN 6
FC601 pixel C6-R0
F601:P 24
FS601 -2603 2503 2708 -2808
FM601 6.24E+15
C
FC611 pixel C6-R1
F611:P 24
FS611 -2602 2502 2708 -2808
FM611 6.24E+15
C
FC621 pixel C6-R2
F621:P 24
FS621 -2601 2501 2708 -2808
FM621 6.24E+15
C
FC631 C6-CENTER PIXEL
F631:P 24
FS631 -26 25 2708 -2808
FM631 6.24E+15
C
FC641 pixel C6-R4
F641:P 24
```

```
FS641 -2651 2551 2708 -2808
FM641 6.24E+15
C
FC651 pixel C6-R5
F651:P 24
FS651 -2652 2552 2708 -2808
FM651 6.24E+15
C
FC661 pixel C6-R6
F661:P 24
FS661 -2653 2553 2708 -2808
FM661 6.24E+15
C
C
C Point detectors
C  AT the center point of each cell radius is = to apperture thickness
C   will need to change radius & z height with diff. aspect ratios
C    x y z  R
FC15  The center pixels in the x=0 plane
F15:P  0 -.03  0.35045   0.002
      0 -.02  0.35045   0.002
      0 -.01  0.35045   0.002
      0  0   0.35045   0.002
      0 .01  0.35045   0.002
      0 .02  0.35045   0.002
      0 .03  0.35045   0.002
FC25  The center pixels in the y=0 plane
F25:P  -.03 0  0.35045   0.002
      -.02 0  0.35045   0.002
      -.01 0  0.35045   0.002
       0  0  0.35045   0.002
      .01 0  0.35045   0.002
      .02 0  0.35045   0.002
      .03 0  0.35045   0.002
C
C TRANSFORM FOR MESH
C
tmesh
 rmesh991:p
 cora991 -0.035 6i 0.035
 corb991 -0.035 6i 0.035
 corc991 0.350449  0.35045
ENDMD
C
C Material
C --------
C Targets
 M1   74000.04p 1 $ Tungsten    rho=19.3 g/cc
C M2 42000.04p 1  $ Molybdenum  rho=10.22 g/cc
C M3 45000.04p 1  $ Rhodium     rho=12.41 g/cc
C M4 82000.04p 1   $ Lead        rho=11.34
C  air (US S. Atm at sea level) density 0.0012 g/cc
M5   7000.04p -0.755636   &
```

```
     8000.04p -0.231475    &
     18000.04p -0.012889
C Si substrate              Rho=2.33 g/cc
C M6 14000.04p 1
C Anode & Filter
M7 29000.04p 1    $ Copper      rho=8.94 g/cc
C
C End of File
```

BIBLIOGRAPHY

[1] Ec Kevles, Bettyann Holtzmann (1996). *Naked to the Bone Medical Imaging in the Twentieth Century*. Camden, NJ: Rutgers University Press. pp. 19–22.

[2] Forster, E., *Equipment for diagnostic radiography*. 1985 Springer Publishing, Chapter 5, pg 65.

[3] Gedeon, Andras. *Science and technology in medicine: an illustrated account based on ninety-nine landmark publications from five centuries*. New York, Springer, 2006, Ch. 67. Pg 345.

[4] Spindt, C. A. 1968. A thin-film field-emission cathode. J. of Appl. Phys. 39. (7), 3504-3505.

[5] Getty, S.A., Auciello, O., Sumant, A.V., Wang, X., Glavin, D. P., Mahaffy, P. R., 2010, Characterization of nitrogen-incorporated ultrananocrystalline diamond as a robust cold cathode material, Proc. of SPIE. 7679, 76794N.

[6] Frutschy, K., Neculaes, B., Inzinna, L., Caiafa, A., Reynolds, J., Zou, Y., Zhang X., Gunturi, S., Cao, Y., Waters, B., Wagner, D., De Man, B., McDevitt, D., Roffers, R., Lounsberry, B. and Pelc, N.J., 2010, High power distributed x-ray source, Proc. SPIE. 7622, 76221H.

[7] Yang, G., Qian, X., Phan, T., Sprenger, F., Sultana, S., Calderon-Colon, X., Kerse, B., Spronk, D., Lu, J., and Zhou, O., "Design and feasibility studies of a stationary digital breast tomosynthesis system," Nuclear instruments and methods in physics research A, S220-S223 (2011)

[8] Grant, E.J., Posada, C.M., Castano, C.H., and Lee, H.K., 2011, Electron field emission particle in cell (PIC) coupled with MCNPX simulation of a CNT-based flat-panel-x-ray source. Proc. of SPIE. 7961, 796108.

[9] Wolbarst, Anthony. Physics of Radiology. Ch.25. Pg 286. Medical Physics Publishing. 2005.

[10] Grant, E. J., Posada, C. M., Castano, C. H., and Lee, H. K. A Monte Carlo simulation study of a flat-panel X-ray source. 2012. Applied Radiation and Isotopes. 70. pgs.1658-1666.

[11] Thompson, A., Lindua, I., Attwood, D., Liu, Y., Gullikson, E., Pianetta, P., Howells, M., Robinson, A., Kim, K., Scofield, J., Kirz, J., Underwood, J., Kortright, J., Williams, G., and Winick, H. X-ray Data Booklet. 2009. LBNL/PUB-490 Rev. 3

[12] Andolina, Valerie, and Shelly Lillé. Mammographic imaging: a practical guide. 3rd ed. Philadelphia: Wolters Kluwer/Lippincott Williams & Wilkins Health, 2011. Print. Pg 239 ch 11

[13] Wang, S., Liu, Z., Sultana, S., Schreiber, E., Zhou, O., and Chang, S., "A novel high resolution micro-radiotherapy system for small animal irradiation for cancer research," BioFactors, 30, 265-270 (2007)

[14] Getty, S.A., King, T.T., Bis, R.A., Jones, H.H., Herrero, F., Lynch, B.A., Roman, P., and Mahaffy, P., "Performance of a carbon nanotube field emission electron gun," Proc. SPIE, 6556, 655618 (2007)

[15] Yamamoto, S., "Fundamental physics of vacuum electron sources," Rep. Prog. Phys., 69, 181-232 (2006)

[16] Chen, Y.C., Zhong, X.Y., Kabius, B., Hiller, J.M, Tai, N.H., and Lin, I.N., "Improvement of field emission performance of nitrogen ion implanted Ultrananocrystalline diamond films through visualization of structure modifications," Diamond & Related Materials. 20, 238-241 (2011)

[17] Koeck, F.A.M., Remanich, R.J., "Field penetration and its contribution to field enhanced thermionic electron emission from nanocrystalline diamond films," Diamond & Related Materials. 15, 2006-2009 (2006)

[18] Chen, Y.C., Tai, N.H., and Lin, I.N., "Substrate temperature effects on the electron field emission properties of nitrogen doped ultra-nanocrystalline diamond," Diamond & Related Materials. 17, 457-461 (2007)

[19] Cheng, H.F., Chiang, H.Y., Horng, .C.C., Chen, H.C., Wang, C.S., and Lin, I.N., "Enhanced electron field emission properties by tuning the microstructure of ultrananocrystalline diamond film," Journal of Applied Physics, 109, 033711 (2011)

[20] Pradhan, D., Lee, Y.C., Pao, C.W., Pong, W.F., and Lin, I.N., "Low temperature growth of ultranoanocrystalline diamond film and its field emission properties," Diamond & Related Materials. 15, 2001-2005 (2006)

[21] Wu, K.,Wang, E.G., Chen, J., and Xu, N.S., "Nitrogen-incorporated distorted nanocrystalline diamond films: structure of and field emission properties," J. Vac. Sci. Technol. B, 17 (3), 1059-1063 (1999)

[22] Auciello, O., Sumant, A. V., "Status review of the science and technology of Ultrananocrystalline diamond (UNCD) films and applications to multifunctional devices," Diamond & Related Materials. 19, 699-718 (2010)

[23] Sankaran, K.J., Chen, H.C., Lee, C.Y., Tai, N.H., and Lin, I.N., "Fabrication of free-standing highly conducting Ultrananocrystalline diamond films with enhanced electron field emission properties," Appl. Phys. Lett. 101, 241604 (2012)

[24] Calderon-Colon, X., Geng, H., Gao, B., An, L., Cao, G., and Zhou, O., "A carbon nanotube field emission cathode with high current density and long-term stability," Nanotechnology. 20, 325707 (2009)

[25] Tolt, Z.L., Mckenzie, C., Espinosa, R., Snyder, S., and Munson, M., "Carbon nanotube cold cathodes for application in low current X-ray tubes," J. Vac. Sci. Technol. B, 26 (2), 706-710 (2008)

[26] Sumant A.V., Auciello, O., Yuan, H.C., Ma, Z., Carpick, R.W. and Mancini, D.C., "Large-area low-temperature Ultrananocrystalline diamond (UNCD) films and integration with CMOS devices for monolithically integrated diamond MEMS/NEMS-CMOS systems," Proc. SPIE, 7318, 731817 (2009)

[27] Marrese, C. 2000. A review of field emission cathode technologies for electric propulsion systems and instruments. ACP IEEE, 4, pg 85-98.)

[28] Fowler R.H. and Nordheim L., "Electron Emission in Intense Electric Fields," Proc. R. Soc. Lond. A 119, 173-181 (1928)

[29] Grider, D., Wright, A. and Ausburn, P., Electron beam melting in microfocus x-ray tubes. J. Phys. D:Appl. Phys. 19 (1986) 2281-2292

[30] Makarova, O. V., Yang, G., Amstutz, P. T., and Tang, C. M. 2008. Fabrication of antiscatter grids and collimators for x-ray and gamma-ray imaging by lithography and electroforming. Microsyst. Technol. 14. 1613-1619.

[31] Pelowitz, D. B. 2008. MCNPX user's manual version 2.6.0. Los Alamos National Laboratory Report, LA-CP-07-1473.

[32] Jeraj, R., Keall, P. J., and Ostwald, P. M. 1999. Comparisons between MCNP, EGS4 and experiment for clinical electron beams. Phys. Med. Biol. 44. (705), 705-717.

[33] Lee, S. W. L., Reece, W. D. 2004. Dose backscatter factors for selected beta sources as a function of source, calcified plaque and contrast agent using monte carlo calculations. Phys. Med. Biol. 49. (583), 583-599.

[34] Posada, C. M., Castaño, C. H., Grant, E. J., Lee, H. K. 2012. Simulation of the electron field emission characteristics of a flat panel x-ray source. J. Vac. Sci. Technol. B. 30. (2). 022201-9.

[35] Poludniowski, G. 2007. Calculation of x-ray spectra emerging from an x-ray tube. Part II. x-ray production and filtration in x-ray targets. Med. Phys. 34. (6), 2175-2186.

[36] Poludniowski, G., Landry, G., DeBlois, F., Evans, P. M., and Verhaegen, F. 2009. SpekCalc: a program to calculate photon spectra from tungsten anode x-ray tubes. Phys. Med. Biol. 54, N433-N438.

[37] Ihsan A, Heo S H, and Cho S O. 2007. Optimization of x-ray target parameters for a high-brightness microfocus X-ray tube. Nucl. Instr. and Meth. B. 264, 371-377.

[38] Berger, M.J. and Seltzer, S. M. 1970. Bremsstrahlung and photoneutrons from thick tungsten and tantalum targets. Phys. Review C 2. (2), 621-631.

[39] Berger M. J., Motz J. W. 2004. X-rays from thick tungsten targets irradiated by 500-50 keV electrons. Nucl. Instr. and Meth. B. 226, 327-334.

[40] Koch H W and Motz J W. 1959. Bremsstrahlung cross section formulas and related data. Rev. Mod. Phys. 31, 920-956.

[41] Tavora L M N, Morton E J, Gilboy W B. 2000. Design considerations for transmission x-ray tubes operated at diagnostic energies. J. Phys. D: Appl. Phys. 33, 2497-2507.

[42] Jensen, K. L. 2009. Space charge effects in field emission: three dimensional theory. J. of Appl. Phys. 107, 14905-14905-9.

[43] Rokhlenko, A., Jensen, K. L., and Lebowitz, J. L. 2010. Space charge effects in field emission: one dimensional theory. J. of Appl. Phys., 107, 14904-14910.

[44] Luginsland, J. W., Lau, Y. Y., Gilgenbach, R. M., 1996. Two-dimensional child-langmuir law. Physical Review Letters. 77. (22), 4668-4670.

VITA

Edwin Joseph Grant was born April 17, 1986, in St. Louis, Missouri. He became interested in Nuclear Engineering while taking introductory engineering classes at East Central College, in Union, Missouri. Edwin graduated with a B.S. in Nuclear Engineering, with Magna Cum Laude honors, in May 2009. He started his M.S. studies, in Nuclear Engineering at Missouri S&T, and graduated during the fall semester of 2010, under Dr. Gary Mueller's advisement. After completing his M.S. degree in Nuclear Engineering, Edwin started his Ph.D. dissertation under the guidance of Dr. Hyoung-Koo Lee. Edwin's dissertation work included fabricating a flat-panel X-ray source at Argonne National Laboratory's Center of Nanoscale Material and testing the device at Missouri S&T. He successfully completed his PhD work during the spring semester of 2014.

Professionally, Edwin joined the American Nuclear Society both as a student and a national member. Also, Edwin was inducted into Alpha Nu Sigma, in the 2009 academic year. For his work at Missouri S&T, Edwin received the Outstanding Graduate Student Award in recognition of his exceptional dedication and commitment to the Nuclear Engineering program. Edwin continued to work in the nuclear engineering field by accepting a position at Knolls Atomic Power Laboratory, as a senior level nuclear component analyst engineer.